Soil Moisture Active Passive (SMAP) Project
Radiometer Brightness Temperature Calibration for the L1B_TB and L1C_TB
Beta-Level Data Products

Prepared by:

(signature)   Aug 4, 2015
Jeffrey Piepmeier   Date
SMAP Radiometer Instrument Scientist
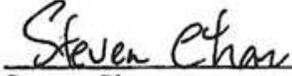
(signature)   Aug 3, 2015
Steven Chan   Date
SMAP L1C_TB Algorithm Lead

Approved by:

(signature)   Aug 4, 2015
Michael Spencer   Date
SMAP Cal/Val Lead
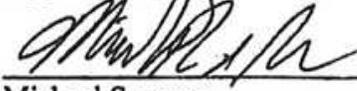
(signature)   Aug 6, 2015
Simon Yueh   Date
SMAP Project Scientist

Paper copies of this document may not be current and should not be relied on for official purposes. The current version is in the SMAP DocuShare library: https://charlie-lib.jpl.nasa.gov/docushare/dsweb/View/Collection-199432

July 30, 2015

JPL D-93978
National Aeronautics and Space Administration

JPL

Jet Propulsion Laboratory
4800 Oak Grove Drive
Pasadena, California 91109-8099
California Institute of Technology

DOCUMENT CHANGE LOG

Revision	Date	Sections Changed	Reason for Change

TBD, TBR, TBS LOG

Section/Page	Description	Due Date

Executive Summary

This report provides analysis and assessment of calibration quality of SMAP radiometer brightness temperatures available in the L1B_TB and L1C_TB beta-level data products. Calibration methods include cold sky and vicarious ocean calibration. Calibration stability is assessed using ocean and Antarctica targets. Geolocation is verified using conventional coastal-crossing analysis. Performance of radio-frequency interference (RFI) mitigation is done using statistical analysis. Overall assessment is performed using comparisons to the Soil Moisture and Ocean Salinity (SMOS) and Aquarius radiometer data.

Results show early calibration using deep space at the start of the mission removed large biases. Geolocation performance meets requirements with ample margin. Antarctica and ocean drift analysis reveals time-varying gain and offset drifts, which are currently corrected by adjusting noise diode calibration coefficients but will need more robust correction in the future. Monthly cold sky calibration validated the drift correction. RFI mitigation is performing very well.

The report finds that the radiometer calibration compares favorably with SMOS over land, ocean, and ice with differences < 1 K; however, comparison with Aquarius over Antarctica leaves some questions on bias. The report notes several limitations and unaddressed areas in the beta-level calibration. These include antenna pattern correction, polarimetric channel calibration, and gain and offset averaging optimization, and separation of noise diode drift from the effects of solar eclipse on front-end losses. Despite these remaining areas, the beta-level product is of sufficient level of maturity that it should be distributed to and used by the larger science and application communities. This beta release also presents an opportunity to enable users to gain familiarity with the parameters and the data formats of the product prior to validation.

1   Introduction

This document summarizes the activities of the SMAP Microwave Radiometer Level 1 Brightness Temperature Calibration Team (the team) during the SMAP Observatory commissioning period and the first three months of operation. The team is delivering Level 1B (time-ordered) and 1C (gridded) brightness temperature data with a beta-level calibration quality for use by the larger science and application communities. These data are distributed through the National Snow and Ice Data Center (NSIDC) Distributed Active Archive Center (DAAC). Both reprocessed data covering the period starting March 31, 2015 and operational forward stream are available.

The team has carried out a series of activities to verify radiometer performance, to adjust calibration coefficients, and to validate the calibration. The activities include geolocation verification, deep space calibration, vicarious calibration, drift monitoring using the ocean surface, drift assessment using Antarctica, and inter-comparison with SMOS and Aquarius radiometer data.

The instrument is performing as expected. Both geolocation accuracy and NEDT meet the project requirements. Comparison with SMOS indicates the beta-level calibration is of sufficient quality to enable reasonable soil moisture retrieval performance. A concise summary of the current performance is listed in Table 1.1. This beta release is expected to provide the science and application communities with data products of sufficient quality to further our understanding of the Earth.

Table 1.1: Beta-level performance of SMAP radiometer.

Parameter	Beta-level	Requirement
NEDT	1.1 K	< 1.6 K
Geolocation accuracy	2.7 km	< 4 km
Land SMAP/SMOS comparison (H pol)	–0.54 K	n/a
Land SMAP/SMOS comparison (V pol)	–0.96 K	n/a

References

Data Products:

Piepmeier, J. R., P. N. Mohammed, J. Peng, E. Kim, G. De Amici and C. Ruf. 2015. *SMAP L1B Radiometer Time-Ordered Brightness Temperatures*. Boulder, Colorado USA: NASA National

Snow and Ice Data Center Distributed Active Archive Center.
http://dx.doi.org/10.5067/1V33MVRRLCCT.

Chan, S., Njoku, E., Colliander, A. 2015. *SMAP L1C Radiometer Half-Orbit 36 km EASE-Grid Brightness Temperatures*. Boulder, Colorado USA: NASA National Snow and Ice Data Center Distributed Active Archive Center. http://dx.doi.org/10.5067/RP9DZ1CC6XNP.

ATBDs:

Piepmeier, J. R. et al. 2015, "SMAP Algorithm Theoretical Basis Document: L1B Radiometer Product," SMAP Project, NASA GSFC SMAP-006, NASA Goddard Space Flight Center, Greenbelt, MD. (https://nsidc.org/sites/nsidc.org/files/files/278_L1B_TB_RevA_web.pdf, 6 MB).

Steven Chan,□Eni Njoku,□Andreas Colliander, "SMAP Algorithm Theoretical Basis Document: Level lC Radiometer Data Product," SMAP Project, JPL D-53053, Revision A, NASA Jet Propulsion Laboratory, Pasadena, CA., December 9, 2014. (http://nsidc.org/sites/nsidc.org/files/files/279_L1C_TB_ATBD_RevA_web.pdf, 1.2MB).

Product Specifications:
Priscilla Mohammed-Tano, "Level 1A Radiometer Product Specification Document," SMAP Project, JPL D-92340, NASA Jet Propulsion Laboratory, Pasadena, CA., July 20, 2015.

Priscilla Mohammed-Tano, "Level 1B Radiometer Product Specification Document," SMAP Project, JPL D-92339, NASA Jet Propulsion Laboratory, Pasadena, CA., July 20, 2015.

Steven Chan and Scott Dunbar, "Level 1C Radiometer Product Specification Document," SMAP Project, JPL D-72545, NASA Jet Propulsion Laboratory, Pasadena, CA., July 14, 2015.

2   Geolocation Assessment

The geolocation requirement for a radiometer footprint is to have knowledge of uncertainty of less than 4 km (interpreted as the not-to-exceed value). The geolocation error is defined as the absolute Cartesian distance between the location reported in the L1B product and an image-processing-derived location in planar geometry. This section provides an assessment of the geolocation performance of the SMAP radiometer system.

The requirement was verified via a comparison of the reported geolocation of the instrument's footprints against the radiometric antenna (or brightness) temperature data at and near coastlines. The assumption underlying this approach is that the antenna temperature will undergo a quick change (from high-to-low) as the instrument's footprint passes from land to water. When the coastline is straight (at the spatial resolution of the footprint) and free of near-shore islands or lakes or rivers, the shape of the change corresponds to the convolution of the antenna's beam gain pattern with a step function, which is mathematically represented as a sigmoid curve. For a reasonably symmetric antenna beam, the midpoint of the sigmoid represents both the largest gradient in temperature and the location of the land/water boundary. This technique has been used successfully to verify the geolocation of heritage satellite-borne microwave instruments (Poe et al., 1990; Poe et al., 2003; Purdy et al., 2006; Poe et al., 2008; Wiebe et al., 2008; Moradi et al., 2013). The novelty here is represented by SMAP full-circle scan, which ensures that whenever a positive (water-to-land) temperature gradients is present within a scan, a corresponding negative (land-to-water) gradient follows (or precedes) within the same or subsequent scan, a few seconds to two and half minutes later.

The algorithm was first "trained" on simulated data, designed to represent a realistic image of the operational measurements. The training showed that the latitude/longitude ranges allowed for a valid detection and the steepness of the sigmoid curve required before a crossing is considered do affect the quality and quantity of the detections. The former is needed to exclude areas where islands, rivers, lakes produce false identifications, the latter to eliminate orbits that are only tangent to the coastline. The results shown here are robust to small changes in the detection parameters.

For this analysis a set of 13 half-orbits was selected to represent overpasses of both N-S and E-W aligned coastlines, along ascending and descending paths. The areas chosen are the Southwest and West coasts of Africa, the East coast of Madagascar, and the West and South coasts of Australia; they are shown in Fig. 2.1 together with the identifiers for the half-orbit files. The common characteristic among these 13 orbits is a near-perpendicular or near-parallel direction of the satellite ground track with respect to the coastline. This ensures that either the edge or the central part of the swath crosses perpendicular to the geographical coastline.
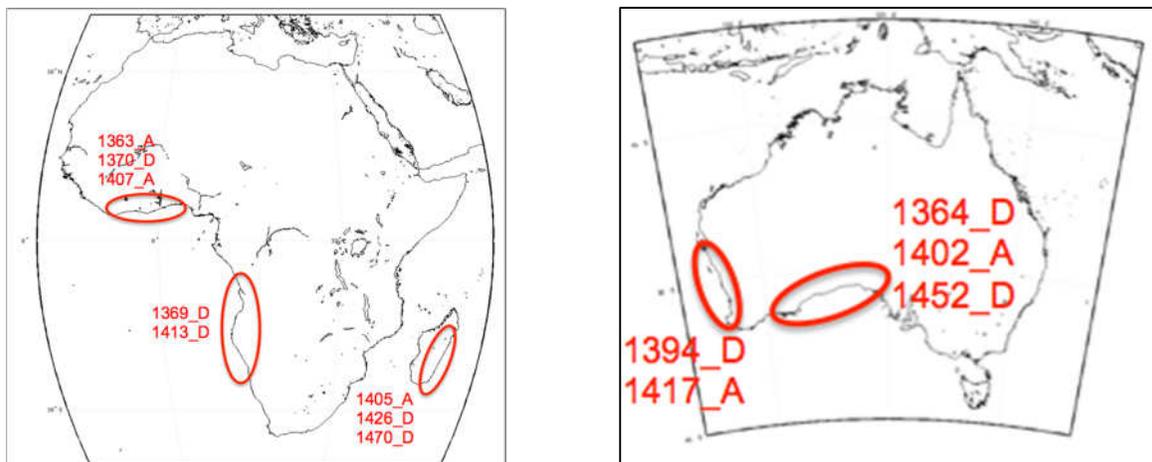
Figure 2.1: Examples of selected ascending/descending half orbits whose ground tracks are either near-perpendicular or near-parallel to geographical coastlines. The resulting transition of the sigmoid curve was used to evaluate the geolocation accuracy of the SMAP radiometer.

The capability of the algorithm was validated against a corresponding set of control orbits from the reported geolocation information. In these orbits, the radiometric data field is replaced by a number which represents the integration of a digital water fraction map (resolution 0.01 deg) with a 2-D Gaussian with major and minor axes that match the projected SMAP antenna footprint; an ocean footprint has value of unity.

For each coastline/orbit combination, the algorithm reports the number of detected crossings and the average absolute distance between each crossing and the nearest true coastline edge, as determined from the finest resolution Global Self-consistent Hierarchical High-resolution Shoreline (GSHHS) map. Table 2.1 shows the results from running the algorithm over the simulated water-fraction data. Each orbit yields at least 68 detections and the uncertainty in the position of the coastline is always smaller than 3 km. The average uncertainty of all detections is 2.35 km – a remarkably small error for footprints that are 35 km wide (HPBW) and sampled every 13 km. Since the water-fraction map and the Gaussian beam pattern are known *a priori* with the highest precision, the error of 2.35 km (less than 7% of footprint size) can be considered the theoretical best achievable by the algorithm on the SMAP footprint. The technique and algorithm discussed here present very good sensitivity to yaw (or clocking) errors, good sensitivity to pitch and roll errors, and almost no sensitivity to errors in the opening angle of the scan cone.

Table 2.1: Determination of geolocation error based on simulated water-fraction data.

Coastline direction	Geographical Area	Orbit #	Coast Geolocation Error (km)	Number of Detected Crossings
N-S	SW Africa	1369_D	2.27	200
	W Australia	1394_D	1.82	78
	Madagascar	1405_A	2.61	150
	SW Africa	1413_D	2.18	192
	W Australia	1417_A	2.13	68
	Madagascar	1426_D	2.08	116
	Madagascar	1470_D	2.61	109
E-W	W Africa	1363_A	2.39	78
	Australia	1364_D	2.01	77
	W Africa	1370_D	2.59	165
	Australia	1402_A	2.96	68
	W Africa	1407_A	2.75	96
	Australia	1452_D	2.16	71
	Average		2.35	

Table 2.2 shows the results of applying the algorithm to a set of operational data, with the geolocation as reported in the L1B files and after applying a small (0.13 deg) counterclockwise yaw correction to the geolocation data. The average uncertainty for the first set of results is 2.73 km, and for the second is 2.45 km. The beta data do not contain the yaw correction and perform as indicated in the first column (i.e., 2.73 km). The actual data, which are inclusive of instrument noise, only increase the geolocation uncertainty to 7% of the footprint.

Table 2.2: Determination of geolocation error after small yaw correction.

Coastline direction	Geographical Area	Orbit #	Coast Geolocation Error (km)	After Yaw Adjustment (km)
N-S	SW Africa	1369_D	2.55	2.77
	W Australia	1394_D	1.55	1.80
	Madagascar	1405_A	3.06	2.10
	SW Africa	1413_D	2.33	2.62
	W Australia	1417_A	2.03	1.75
	Madagascar	1426_D	2.18	1.57
	Madagascar	1470_D	3.48	3.10
E-W	W Africa	1363_A	3.05	2.96
	Australia	1364_D	3.09	2.13

	W Africa	1370_D	3.13	2.85
	Australia	1402_A	3.54	3.28
	W Africa	1407_A	2.75	2.37
	Australia	1452_D	2.67	2.49
	Average		2.73	2.45

References

Moradi, I., et al., "Correcting Geolocation Errors for Microwave Instruments aboard NOAA Satellites", *IEEE TGRS*, 51, 3625, June 2013.

Poe, G.A., and R. W. Conway, "A study of the geolocation errors of the special sensor microwave/imager (SSM/I)," *IEEE TGRS*, 28, 5, 791–799, September 1990.

Poe, G.A. et al., "Conical Microwave Imaging/Sounding: Geo-location Error Analysis", 2003 (NPOESS Internal Government Study, unpublished)

Poe, G.A., et al., "Geolocation error analysis of the special sensor microwave imager/sounder," *IEEE TGRS*, 46, 913–922, April 2008.

Purdy, W. E., et al., "Geolocation and pointing accuracy analysis for the WindSat sensor," *IEEE TGRS*, 44, 496–505, March 2006.

Wiebe, H., G. Heygster and L. Meyer-Lerbs, "Geolocation of AMSR-E data," *IEEE TGRS,* 46, 3098–3103, October 2008.

3 Initial Bias Removal in T_{ND}

The SMAP radiometer internal calibration is described in Sections 5.4–5.6 of the SMAP radiometer L1B ATBD. The antenna temperature (T_A, referenced to the feedhorn) is calibrated by using the reference load and the noise source. In addition, the effects of the losses of RF components/cables and impedance mismatch are corrected. The error in the calibrated T_A is primarily due to uncertainty in the noise source measurement during pre-launch calibration based on the analysis listed in Table 2.1 in Piepmeier et al., 2013. Therefore, the brightness temperature of the noise source (T_{ND}) was adjusted within the first week after launch and power-on to remove the initial bias. The latter was possible because before the reflector was deployed starting on Feb 18, 2015, the radiometer was powered on with the feedhorn pointed to zenith away from Earth viewing deep space. Without the effect of the reflector, the cold sky was used as the external calibration target to remove the initial bias in T_{ND}.

Figure 3.1(a) shows the initial radiometer T_A measurement after first power-on. Galaxy signature can be seen clearly in the measurements, and its shape matches the simulation very well. But there are biases on both V-pol and H-pol measurements comparing to the expected antenna temperature (simulation). Assuming the bias is only caused by the uncertainty in T_{ND}, adjustment to T_{ND} has been performed and the adjustment is given by

$$\Delta T_{ND} = L_{RF}^{-1} \left(\frac{C_{ref+ND} - C_{ref}}{C_A - C_{ref}} \right) \left(T_{A,exp} - T_A \right)$$

where L_{RF} is the loss of the radiometer RF front end. Count values C_x ($x = A$, ref, $ref+ND$) are the radiometer output counts for the antenna, reference load, and reference load with noise diode on states, respectively.

After T_{ND} adjustment in Fig. 3.1(b), the biases in calibrated TAs were decreased from –4.44 K and 1.46 K to 0.21 K and 0.15 K for V- and H-pol measurements, respectively.
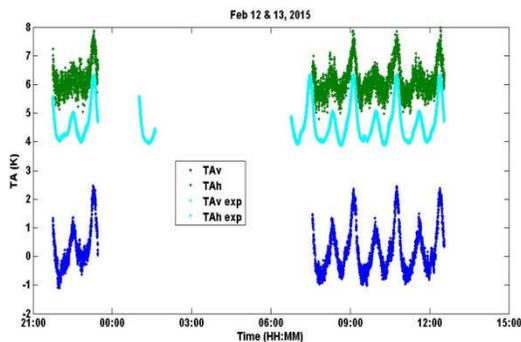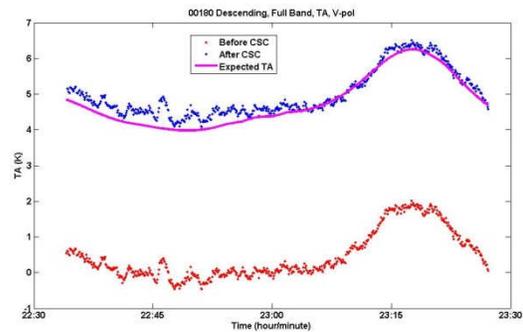
(a)   (b)

Figure 3.1: Cold sky calibration prior to reflector deployment. (a) Part of the radiometer measurement and simulation. (b) V-pol antenna temperature before/after cold sky calibration.

Reference

J.R. Piepmeier et al., 'Aquarius Radiometer Post-Launch Calibration for Product Version 2', Aquarius project document, AQ-014-PS-0015, Feb 19, 2013. [online] Available at http://podaac.jpl.nasa.gov/aquarius.

4   Drift Removal in T_{ND}

After the radiometer was powered on, global ocean (blue area in Fig. 4.1) has been being used as an external target to monitor calibration bias and drift in T_{ND}.
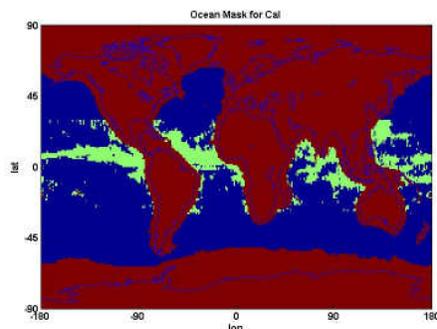
Figure 4.1: Ocean mask for monitoring T_{ND} calibration bias and drift.

It was observed that the measured T_A's were drifting comparing to the ocean L-band GMF model (Yueh et al., 2013). Besides drift, there were also biases. The biases are likely due in part to inaccurate galactic T_B model, standing wave between the reflector and radiometer front end, and error in antenna pattern. The drift and bias from Apr 1 to Jun 22, 2015 are shown in Fig. 4.2, where $\delta\, T_A <T_{A,measured} - T_{A,modeled}>_{day}$ are the daily averaged differences between measured and expected antenna temperatures. The biases on Apr 1, 2015 are 0.11 K and –0.55 K for V- and H-pol measurements, respectively. The difference $\delta\, T_A$ had been drifting at almost constant rate before May 27, 2015, and then became constant which means that the radiometer is stable (at least temporarily).
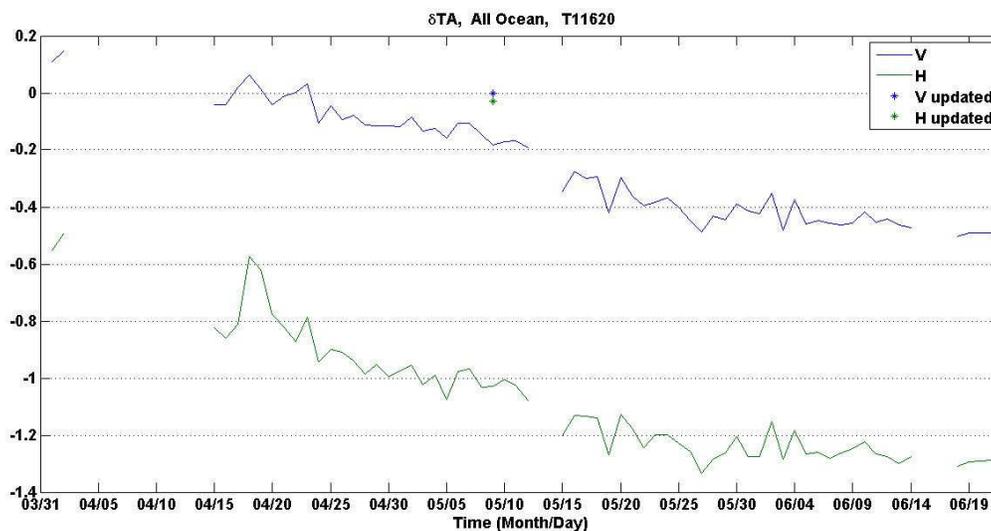
Figure 4.2: Radiometer T_A calibration bias and drift.

In order to remove the drift or time-varying bias, similar approach as that used for removing initial bias is applied. The drift or time-varying bias is assumed to change at constant rate, and linear regression is applied to derive δ T_A for the day without or not enough normal science data. Daily updated T_{ND} is used for L1A data processing to get L1B data if drift exists. A test was performed using a half-orbit data on May 9, 2015, the calibrated antenna temperatures for both V- and H-pol measurements were close to the expected antenna temperatures, and the biases were reduced from –0.18 K (V-pol) and –1.03 K (H-pol) to 0.00 K (V-pol) and –0.03 K (H-pol). When the radiometer became stable, T_{ND} for the day May 27, 2015 was used.

Reference

S.H. Yueh et al., "L-Band Passive and Active Microwave Geophysical Model Functions of Ocean Surface Winds and Applications to Aquarius Retrieval," *Geoscience and Remote Sensing, IEEE Transactions on*, v. 51, no. 9, pp.4619–4632, Sept. 2013. doi: 10.1109/TGRS.2013.2266915

5 Front-End Loss Effects

5.1 Thermal Stability: Front-end RF Components and SAR Transmitter

Figure 5.1(a) below shows the RF element temperatures during a planned bake-out. Before bake-out the SAR transmitter was also turned off. The global δT_A (Fig. 5.1(b)) over the ocean shows two separate impacts due to these events.

1. A drop in the measured T_A with respect to the modeled T_A when the SAR transmitter was turned off.
2. A rise in the measured T_A with respect to the modeled T_A when the RF bake-out was occurring.
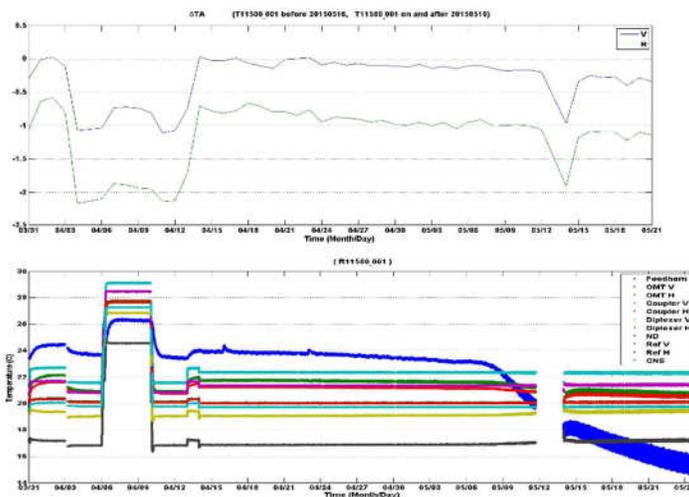
Figure 5.1: (a) Daily averaged global ocean δT_A indicating T_A biases due to SAR transmitter being turned off (Apr 3) and on (Apr 13) and radiometer bake-out (Apr 6 to Apr 10). (b) Front-end temperature of the RF components over the same period.

The T_A bias due to the SAR transmitter being turned off is an expected occurrence from pre-launch data analysis. The radiometer data calibration parameters have been set based on the SAR transmitter being turned on. On July 7, 2015 (not shown in figure), the SAR transmitter encountered an anomaly that turned off the radar, causing a shift in radiometer calibration. The beta-release data compensates for this anomaly by adjusting the reference load calibration values post July 7, 2015 to account for the offset bias.

The second front-end impact observed from Figure 5.1 is the change in T_A bias with change in the RF temperature components. The front-end thermal calibration coefficients cannot completely compensate for the changing thermal environment of the RF components. Currently the beta-release data has not updated the thermal coefficients to reflect the impact of this event. The case presented above is an extreme case impacting the T_A bias.

5.2   Radome and Reflector Impact on T_A Stability

The impact of the radome and reflector front-end loss factors on the antenna temperatures was evaluated by comparing measured T_A over the ocean with modeled T_A over the same region. Ideally, the global δT_A should be independent of the radome/reflector temperature at a particular orbit location.

Figure 5.2 shows the averaged δT_A with respect to various radome temperatures. It should be noted that the radome and reflector temperatures are thermally modeled and not directly measured by the SMAP observatory. As noted in the figure, there is an effect of the radome temperature on the T_A value measured.
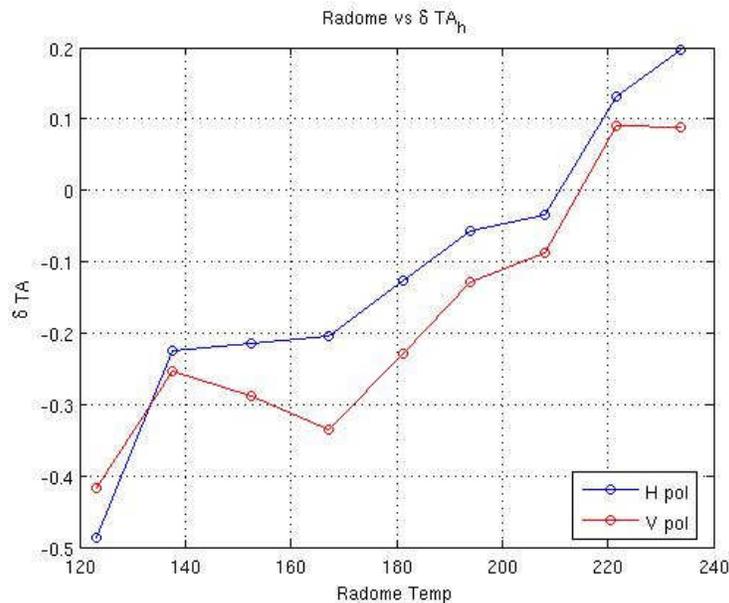
Figure 5.2: Averaged difference between measured T_A and modeled T_A over the ocean with respect to modeled radome temperature derived over a two month period.

Table 5.1 represents the antenna temperature sensitivity and approximate loss calculated from the H- and V-pol measurements.

Table 5.1: Radome and Reflector antenna temperature sensitivity
and loss

	dT_A/dT (K/K)	Effective Loss
H pol – Radome	5.1e-3	1.005
V pol – Radome	4.3e-3	1.004
H pol – Reflector	0.012	1.01
V pol – Reflector	0.012	1.01

Figure 5.3 show the averaged δT_A with respect to various reflector temperatures. The reflector seems to have more of an impact on the T_A values measured. Both radome and reflector sensitivity measurements were made with data from the months of May and June. The spacecraft entered into eclipse during those months, allowing for larger dynamic temperature changes. The radome and reflector temperature variations are highly correlated and it is impossible to completely separate out the impact of the front-end losses between the two.
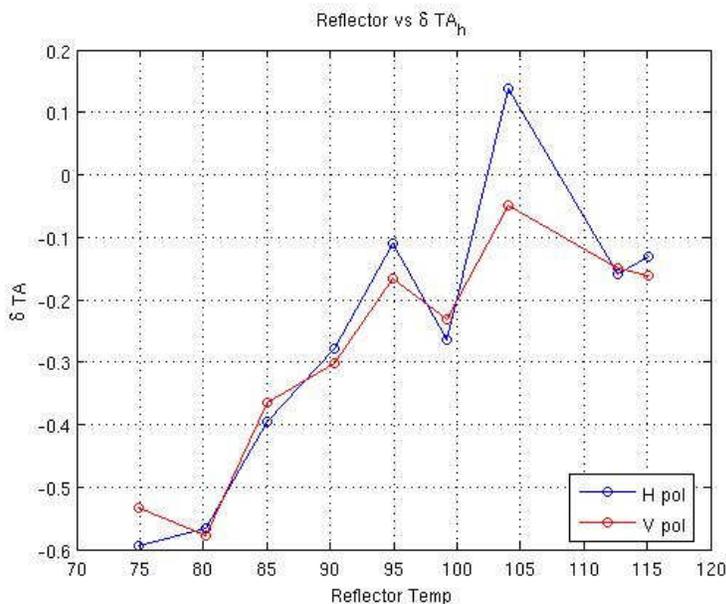
Figure 5.3: Averaged difference between measured T_A and modeled T_A over the ocean with respect to modeled reflector temperature derived over a two month period.

Caveat:

Currently the beta release data does not include an updated correction for the radome/reflector front-end loss dependency. It is likely the noise source correction described previously is compensating for radome/reflector loss misspecifications. Due to the high correlation between

reflector and radome temperature changes, further analysis is required to assign a calibration correction in the front-end loss elements. The radome and reflector temperatures are also orbit and latitude dependent, potentially causing geographic ocean T_A biases to get aliased into the analysis. These factors must be considered before applying a radome/reflector correction.

6 Full Dynamic Range Calibration

6.1 Cold Sky Calibration (CSC)

The celestial sky at L-band (Fig. 6.1) is used for the post-launch empirical calibration of the radiometer because it offers well-characterized T_B, spatial homogeneity over large regions and very high temporal stability. It is also free of RFI. Cold-sky calibration (CSC) has been used for two purposes: (1) to determine the instrument bias and its stability in time and (2) to assess the accuracy of the antenna pattern.
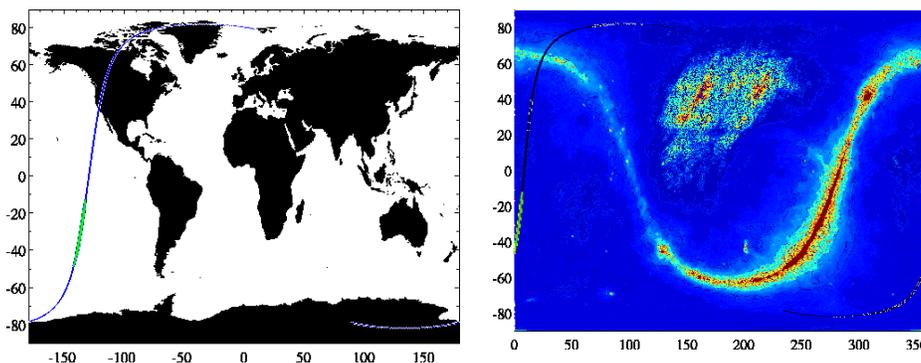
Figure 6.1: SMAP spacecraft ground track over the Earth (left) and the celestial sky (right, color reports the cold sky T_B) for the CSC on Jun 30 2015. The green section of the track reports the 5-min calibration period used to derive the radiometer bias.

6.1.1 Nominal CSC to Assess Radiometer Bias and Temporal Stability

Nominal CSC's are performed with the spacecraft above open ocean to limit uncertainty due to the land emission model (Fig. 6.1). Three CSC were performed on Apr 23, May 27 and Jun 30, 2015. Examples of time series of measured T_A and modeled T_A are reported in Fig. 6.2 and show the good agreement between the model and the observations to within a bias (constant offset between the curves for observed and modeled T_A). Because of the large spatial coverage of the scan, it is common to have part of the scan getting close to or crossing the galactic plane and strong celestial sources. This results in larger temporal variation for some scan angles (cf. left vs. right panel in Fig. 6.2).
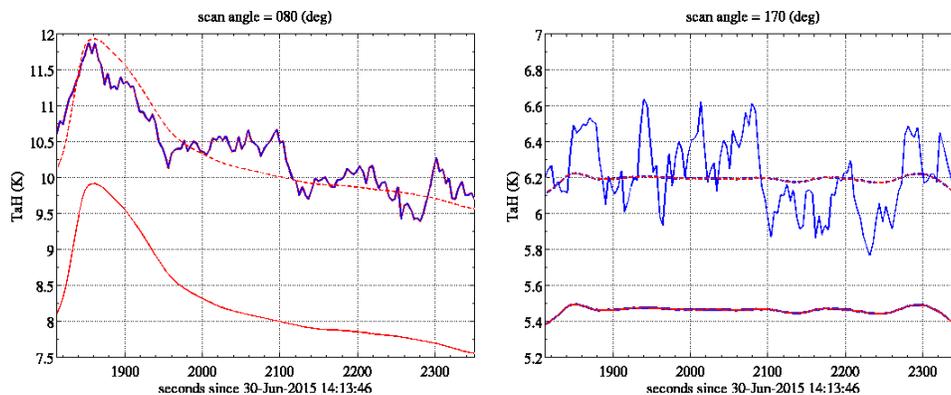
Figure 6.2: Time series of (blue) observed and (red) simulated T_A in horizontal polarization during the CSC on Jun 30, 2015 at a scan angle of (left) 80° and (right) 170°. SMAP observations have been averaged over a 5° scan angle range and over 20s. The simulations are reported (red, plain) unadjusted and (red dashed) with an added constant offset (i.e. bias) to match the observations on average over the 5 min window of the CSC.

The bias varies with the scan angle, as reported in Fig. 6.3, with variations between V-pol and H-pol anti-correlated (see also the bias in first Stokes more stable with the scan angle). Overall, SMAP observations are found warmer than the simulation by about 1.2 K +/–0.7 K. It is not known for now why the bias varies with the scan angle. All three nominal CSC show similar results. The bias is stable between the three CSC and varies by +/–0.2K at most scan angles.
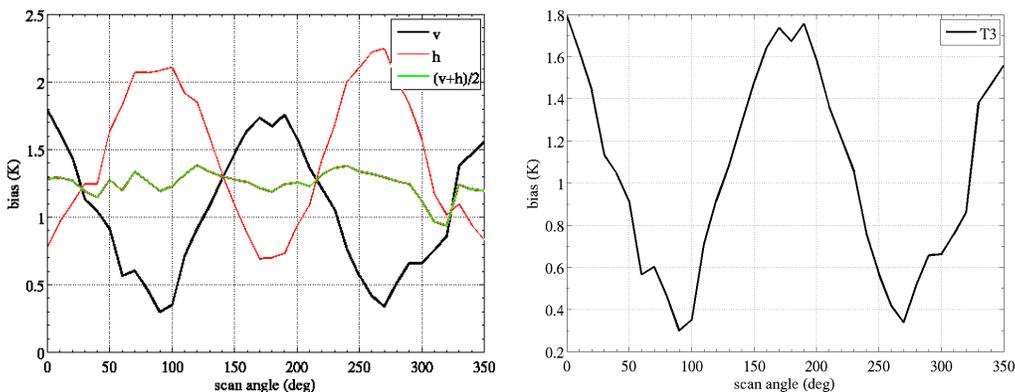
Figure 6.3: T_A bias vs. scan angle for the CSC on Jun 22, 2015 for V-pol (black), H-pol (red) and the first Stokes parameter (green). Same for the third Stokes parameter (right).

6.1.2 Ocean-land Crossing CSC to Assess Antenna Pattern Accuracy

A special CSC designed to assess the uncertainty on the antenna pattern was conducted on Jun 22, 2015 with the spacecraft flying over a transition between ocean and land (Amazonian rain forest, Fig. 6.4). The CSC uses the very large contrast in T_B between water and land to assess the fraction of antenna power pointing toward the Earth. The very good agreement between model and observations (Fig. 6.5) point to accuracy better than 1% on the Earth power ratio. The vertical polarization appears to have a slightly larger uncertainty. Further characterization of the uncertainty is ongoing.
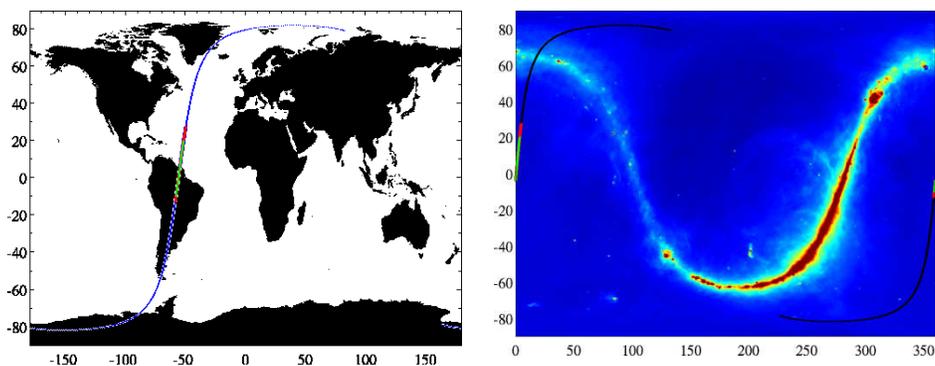
Figure 6.4: SMAP spacecraft ground track over the Earth (left) and the celestial sky (right, color reports the cold sky T_B) for the ocean-land crossing CSC on Jun 22, 2015. The green section of the track reports the 5-min calibration period used to derive the instrument bias.
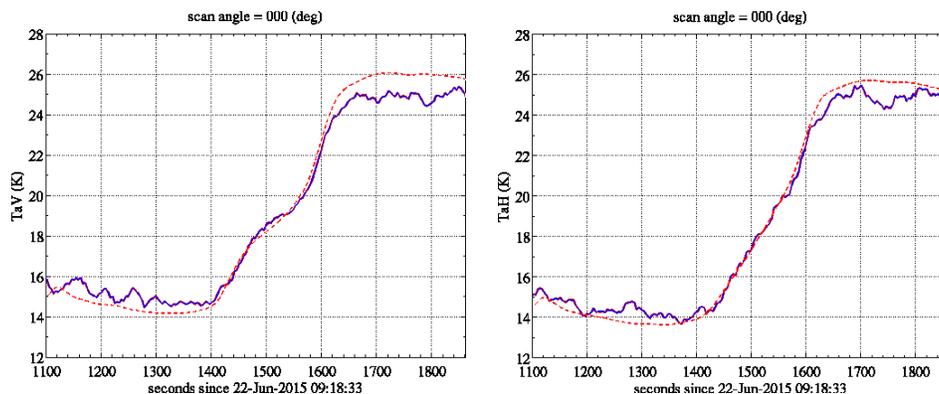
Figure 6.5: Time series of (blue) observed and (red) modeled T_A in (left) vertical and (right) horizontal polarization during the ocean-land crossing CSC on Jun 22, 2015 at a scan angle of 0°. SMAP observations have been averaged over a 5° scan angle range and over 20 sec time. The simulations are reported with an added constant offset to match the observations on average over the 5 min window of the CSC.

6.2   Comparison with SMOS

Inter-comparison of SMAP T_B with SMOS T_B can be a useful tool for radiometer calibration. SMOS and SMAP have an equatorial overpass time of 6 AM (SMOS-ascending; SMAP-descending). Collocated and concurrent measurements provide a consistency check on the calibration: if the T_B's from two L-band satellites (e.g. SMAP and SMOS) are acquired at the same time and location, then they should be similar.

In order to minimize inter-comparison errors associated with temporal changes in soil moisture and temperature, a maximum time window between the two satellite observations of 30 min was used in this analysis. Furthermore, only those SMAP and SMOS observations (both H- and V-pol measurements) whose footprints were less than 1 km apart were considered.

Microwave observations from the SMOS mission were reprocessed to approximate SMAP microwave radiometer observations made at a constant incidence angle of 40.0°. Only the alias-free portions of the SMOS field-of-view were used in the comparison. Additionally, the alias-free portions of the swath provide brightness temperatures with the lowest NEDT. SMOS data version v620 was used for the analysis.

This comparison was done with beta-release SMAP data. Figures 6.6 (a)-(b) shows the SMAP and SMOS observations over land for the period of May 6-July 14, 2015. The SMAP brightness temperatures show a very strong correlation with the SMOS observations. Based upon these results we concluded that the SMAP brightness temperatures are within the radiometer noise levels for both the polarizations. Some of the scatter in the inter-comparison is likely due to the presence of RFI in either or both of the SMAP or SMOS observations. Land surface heterogeneity of the footprint can also result in some scatter.

(a)   (b)
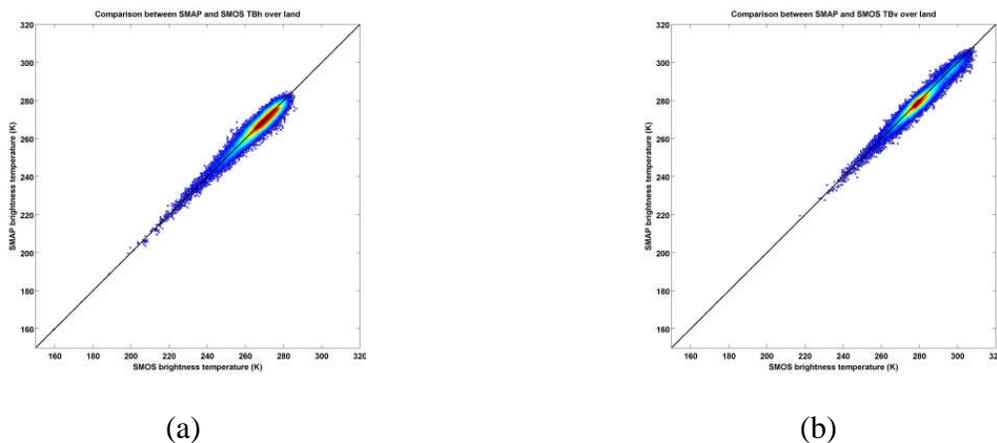
Figure 6.6: Density plot of the comparison between SMAP T_B and SMOS T_B over land for (a) H-pol, and (b) V-pol. Scale adjusted for land T_B.

In addition, we extracted the equivalent data set over oceans, which are also plotted in Figs. 6.7 (a)-(b). These combined results provide strong evidence of the relative calibration of SMAP and SMOS over a wide range of targets. The SMAP brightness temperature compared well with SMOS observations over oceans. The comparison between SMAP and SMOS brightness temperature shows a strong linear relationship. Statistical analysis results are summarized in Table 6.1.

(a)   (b)
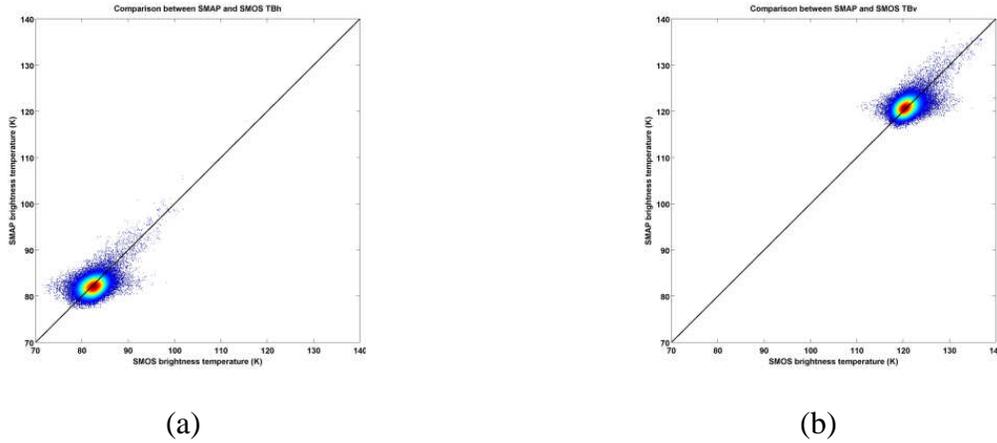
Figure 6.7: Density plot of the comparison between SMAP T_B and SMOS T_B over ocean for (a) H-polarization, and (b) V-polarization. Scale adjusted for ocean T_B.

Table 6.1: Statistics for SMAP and SMOS comparison.

		RMSD (K)	**R**	**Bias [SMAP-SMOS] (K)**
H pol	Land	3.34	0.9708	–0.54
	Ocean	2.32	0.4991	–0.22
	Overall	2.61	0.9994	–0.30
V pol	Land	3.14	0.9746	–0.96
	Ocean	2.15	0.5505	0.16
	Overall	2.44	0.9995	–0.12

In short, the analyses conducted here show that the SMAP T_B and SMOS T_B are nearly identical over the full range of T_B. A small adjustment over land may be considered after all other calibration issues have been addressed.

6.3   Comparison with Aquarius

Gridded products over Antarctica were used to compare the high-end calibration of the SMAP radiometer to Aquarius. Antarctica was used due to its high temporal stability and large-scale spatial homogeneity at L-band for location away from the edge of the continent, i.e. away from topography and possible melt events (Brucker et al., 2014a). The polar gridded Aquarius data (Brucker et al., 2014b) were used for Aquarius middle beam and outer beam to interpolate Aquarius surface T_B at SMAP incidence angle of 40 deg.

The maps in Fig. 6.8 report the differences between SMAP T_B and Aquarius T_B for one week. The differences inland are fairly homogeneous and around 4.5 K in V-pol and 2.5 K in H-pol. The differences appear constant for $T_B > 200$ K in V-pol, but they increase from 2.5 K to 4.5 K in H-pol.
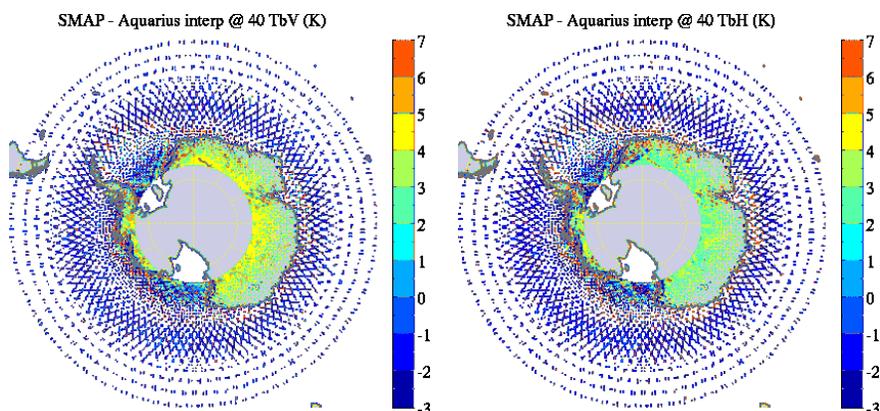
Figure 6.8: Map of differences in weekly surface T_B measured by SMAP and Aquarius in (left) H-pol and (right) H-pol. Aquarius data have been interpolated at an incidence of 40 deg from observations from the middle and outer beams.
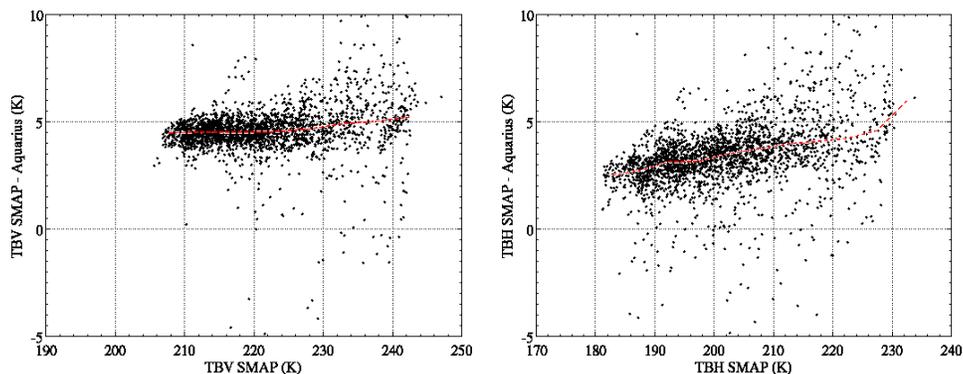
Figure 6.9: Scatter plot of the difference in SMAP surface T_B and Aquarius surface T_B vs. SMAP surface T_B over Antarctica in (left) V-pol and (right) H-pol. The red line reports the median of the differences in SMAP T_B bins.

The comparisons over Antarctica are not in agreement with comparisons over land at lower latitudes, which show smaller bias at the high end of T_B. Fig. 6.10 reports T_B comparisons for one week of SMAP and Aquarius observations collocated within 30 minutes and 20 km of each other at latitudes less than 60 deg. The larger bias observed over Antarctica has been traced to a difference of a few Kelvins in the corrections for the atmospheric effects between SMAP and Aquarius. The difference over ocean is uncertain within a few Kelvins because of (1) the difference in incidence angle between SMAP and Aquarius and (2) the intensity of the reflected galaxy for both instruments.
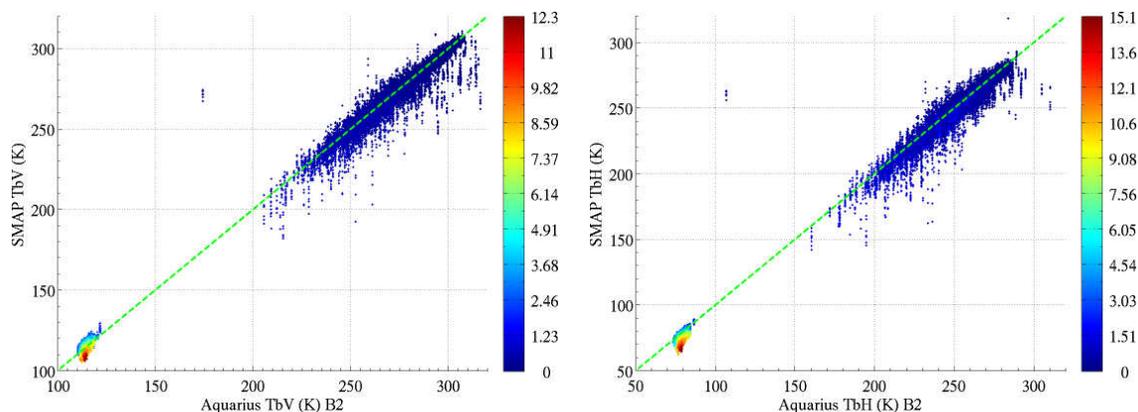
Figure 6.10: Scatter plot of SMAP T_B versus Aquarius T_B for 1 week of collocations within 30 minutes and 20 km in (left) V-pol and (right) H-pol. The color scale reports the amplitude of the correction for the reflected galactic signal applied to the SMAP observations.

Reference

L. Brucker, E. P. Dinnat, and L. Koenig, "Weekly-gridded Aquarius L-band radiometer/scatterometer observations and salinity retrievals over the polar regions – Part 2: Initial product analysis," The Cryosphere, vol. 8, no. 3, pp. 915–930, 2014.

L. Brucker, E. Dinnat, and L. Koenig. 2014. *Aquarius L3 Weekly Polar-Gridded Brightness Temperature and Sea Surface Salinity.* Version 4. Boulder, Colorado USA: NASA National Snow and Ice Data Center Distributed Active Archive Center. http://dx.doi.org/10.5067/Aquarius/AQ3_TB.004.

7   Faraday Rotation Correction Assessment

Faraday rotation, a change in polarization that occurs as electromagnetic waves propagate through the ionosphere, can be significant at L-band (Le Vine and Abraham, 2002). Knowledge of the change in polarization is important because the science retrievals are based on the polarization of the signal at the surface (e.g. the "single channel" algorithm in the retrieval of soil moisture which assumes horizontal polarization (Entekhabi et al., 2014)). The amount of Faraday rotation is quite variable, changing with orbital position, local time of day, and with solar and geomagnetic activity. It also depends on the orientation of the propagation path with respect to the local Earth magnetic field, which in the case of a conical scanner such as SMAP changes rapidly.

Fortunately, the rotation angle can be measured at the spacecraft with a polarimetric radiometer such as is flown on SMAP. In the ideal case, the ratio of the third Stokes parameter, T_3, to the second Stokes parameter, $Q = T_V - T_H$, is proportional to the tangent of twice the angle of Faraday rotation (Yueh, 2000) and can be used to retrieve the rotation angle. The concept was demonstrated over ocean scenes with Aquarius (Le Vine et al, 2013). However, the realities of real antennas such as cross-pol coupling and wide footprints can cause errors in the retrieval (Le Vine et al., 2007; Le Vine et al., 2011) and the potential for additional uncertainty is introduced in the case of SMAP by the conical scan geometry and the requirement to operate over land with highly variable scenes.

A preliminary assessment using pre-beta release data has been made of the efficacy of using the third Stokes parameter to measure Faraday rotation in the SMAP configuration. The analysis consists of retrieving the rotation angle from the measured values of T_V, T_H and T_3 and comparing these with theory using the SMAP simulator and the local Earth magnetic field and total electron content (TEC) from the IGS corrected for the altitude of SMAP.

A first check has been made comparing the Faraday rotation angle retrieved over open ocean with theory. This is an important check because ocean is a scene where the algorithm is expected to work well. Any issues here might indicate issues with the radiometer output. Figure 7.1 (left) shows the location of an example scan over the ocean. On the right is shown the retrieved Faraday rotation (blue) and a version smoothed over 20 samples (red). The bold (blue) line is theory obtained using the TEC predicted by the IGS. Figure 7.2 is another example over the ocean. On the left is shown the Faraday rotation angle retrieved along the track of the spacecraft. The values plotted without concern for overlap (i.e. the new value replaces the previous result if there is overlap). On the right are the scan average value (blue) and the theoretical value obtained using the IGS value for TEC.
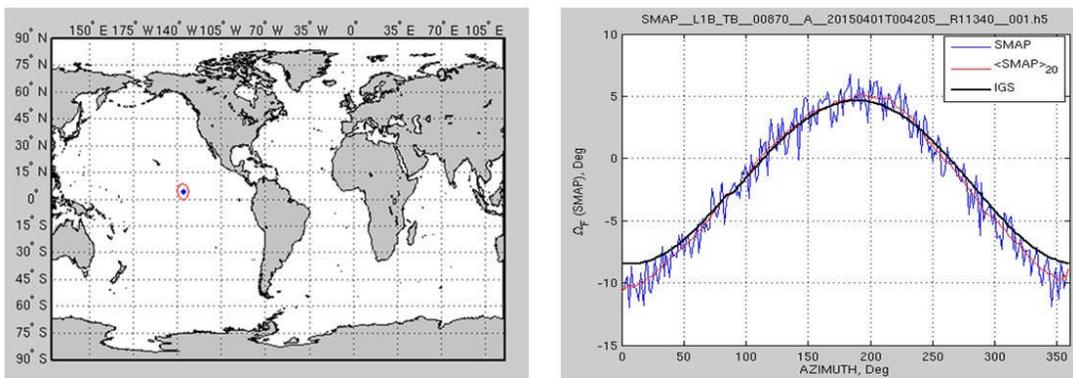
Figure 7.1: Retrieved Faraday rotation angle for an individual scan over the ocean
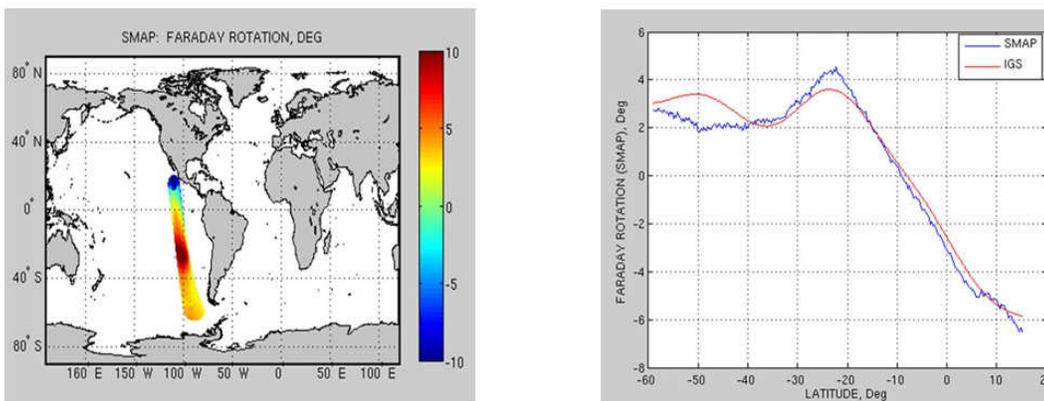
Figure 7.2: Retrieved Faraday rotation angle over the ocean averaged along track.

The retrievals of Faraday rotation angle over ocean look reasonable although the effects of noise are apparent. Retrievals over land are subject to known errors associated with spurious T_3 over inhomogeneous scenes (Le Vine et al., 2011) and studies being conducted for SMAP indicate large errors are possible over dense vegetation such as forests (Le Vine, Abraham and Peng, 2015). Work is continuing to check more cases and to document the problems over land. Techniques to reduce the noise in the estimates are also being studied.

References

D. Entekhabi et al., *SMAP Handbook: Soil Moisture Active Passive*, National Aeronautics and Space Administration, Jet Propulsion Laboratory, Pasadena, California, Ch. 4, pg 55, July, 2014.

IGS 2015: http://www.igs.org

D. M. Le Vine and S. Abraham, "The Effect of the Ionosphere on Remote Sensing of Sea Surface Salinity From Space: Absorption and Emission at L Band", *IEEE Trans. Geosci. and Remote Sens.*, vol. 40, no. 4, pp 771–782, April 2002.

D. M. Le Vine, S. D. Jacob, E. Dinnat, P. de Matthaeis, S. Abraham, "The Influence of Antenna Pattern on Faraday Rotation in Remote Sensing at L-band", *IEEE Trans. Geosci. & Remote Sens.*, vol. 45, no. 9, pp 2737–2746, September 2007.

D.M. Le Vine, E.P. Dinnat, S. D. Jacob, S. Abraham and P. de Matthaeis, "Impact of Antenna pattern on measurement of the third Stokes parameter from space at L-band", *IEEE Trans. Geosci. Remote Sens.*, vol 49, no. 1, pp. 406–414, January 2011.

D.M. Le Vine, S. Abraham, C. Utku and E.P. Dinnat, "Aquarius Third Stokes Parameter Measurements: Initial Results", *IEEE Geosci. and Remote Sens. Letters*, vol.10, no. 3, pp 520–524,May 2013.

D. M. Le Vine, S. Abraham and J. Peng, "Faraday Rotation Correction for the SMAP Radiometer", *IEEE Trans. Geosci. and Remote Sens.*, submitted June, 2015.

S. Yueh, "Estimates of Faraday Rotation with Passive Microwave Polarimetry for Microwave Remote Sensing of Earth Surfaces", *IEEE Trans. Geosci. and Remote Sens*., vol. 38, no. 5, pp 2434–2438, 2000.

8 Reflected Galaxy Correction Assessment

Figure 8.1 shows the uncorrected T_A (V-pol only) for a representative set of consecutive descending orbits. The data are segregated by the antenna scan angle, which indicates whether the instrument is pointing forward or backward respect to the orbital velocity vector, and binned on a 0.25-deg grid. Within each grid cell the data are weighted by the inverse of their distance to the center of the grid cell.
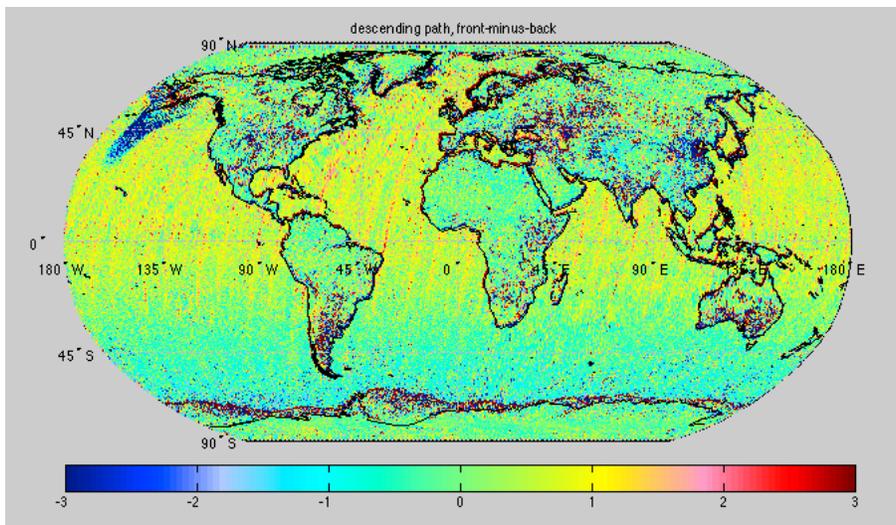
Figure 8.1: Uncorrected T_A (V-pol) for days 20150411-to-20150420, which cover slightly more than one full SMAP cycle. Data are segregated by ascending/descending orbital path (only descending shown here) and by forward/backward respect to orbital motion, then averaged in 0.25 deg bins. The difference between the forward-looking data and the backward-looking data is used to eliminate the DC component of any signal, and highlight differences.

The stripes along the ground tracks of the orbits are caused by the reflection of the galaxy into the main antenna beam. Under appropriate conditions of illumination time-of-day, and reflecting angle, the difference between the apparent antenna temperature of a pixel as seen in a forward or in a backward look reaches up to 3 K. The bright highlighting of coastlines produced by this analysis is discussed in details in Section 10.

The contribution of the reflection of the galaxy off the surface of the Earth and into the main beam of the SMAP has been modeled as the convolution of a map of the radio galaxy at 1420 MHz with a circularly symmetric averaged beam pattern. This is further convolved with the smearing introduced by a 7 m/s wind over the ocean surface. The net effect is equivalent to a smoothed (lacking all bumps and local maxima/minima of the true beam pattern) and wider (about 1.3 times larger HPBW) antenna beam.

Application of this model to the data of Fig. 8.1 produces the map shown in Fig. 8.2. While the forward-minus-backward differences remain, their amplitudes are reduced by a factor of 3 or 4, indicating that the approach is fundamentally sound but in need of further refinements.

One such improvement could be the indexing of the effective beam pattern profile by the clock angle of the scan while at the same time using the asymmetric 'real' beam pattern for the convolution with the wind speed and galactic signal. A further step could modify the surface reflectivity to account for varying wind speed. Both approaches are under consideration and will be further explored.
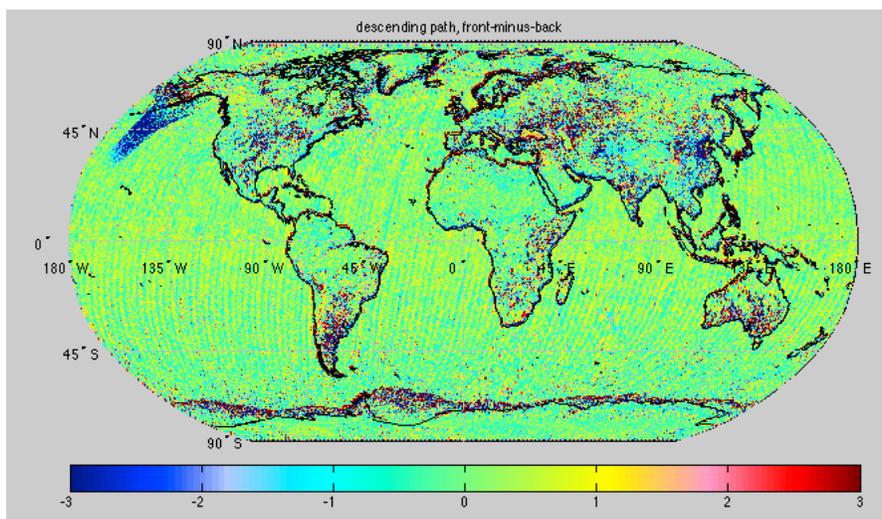
Figure 8.2: The same data as in Fig. 8.1, but converted to T_B (V-pol) using the most recent model of reflected galactic signal. The striping is still visible but it is reduced by a factor of about 3 from what was shown in Fig. 8.1. Front/back segregating, gridding and averaging are applied equally here as in this figure and Fig 8.1.

9 Radio-Frequency Interference Assessment

As described in (Piepmeier et al, 2014), the SMAP radiometer includes a digital backend to improve the detection and filtering of radio frequency interference (RFI). The digital backend produces two independent data streams from SMAP observations (Fig. 9.1): a "fullband" product representing 32 samples of the entire observed bandwidth resolved at ~ 300 μsec time resolution (i.e. each radar pulse repetition interval – PRI) and a "subband" product consisting of 16 frequency channels resolved in eight time samples at ~ 1.2 msec time resolution (4 PRI's). Each of these data streams is accompanied by information on its first, second, third, and fourth integrated moments, enabling computation of the kurtosis of each as well. This information is available to ground processing for both the horizontally and vertically polarized channels and for the third and fourth Stokes parameters. As shown in Fig. 9.1, the final footprint level antenna temperature is computed in ground processing by averaging over the 8-time-by-16-channel antenna temperature spectrogram, excluding any "pixels" in the spectrogram flagged by any RFI detection algorithms. Discarding pixels from the spectrogram in the footprint integration degrades the radiometer sensitivity. The radiometer quality flag includes flags for an excessive degradation in radiometer sensitivity and an excessive detected RFI level. Additional discussion of these flags is provided in the Quality Flags section.
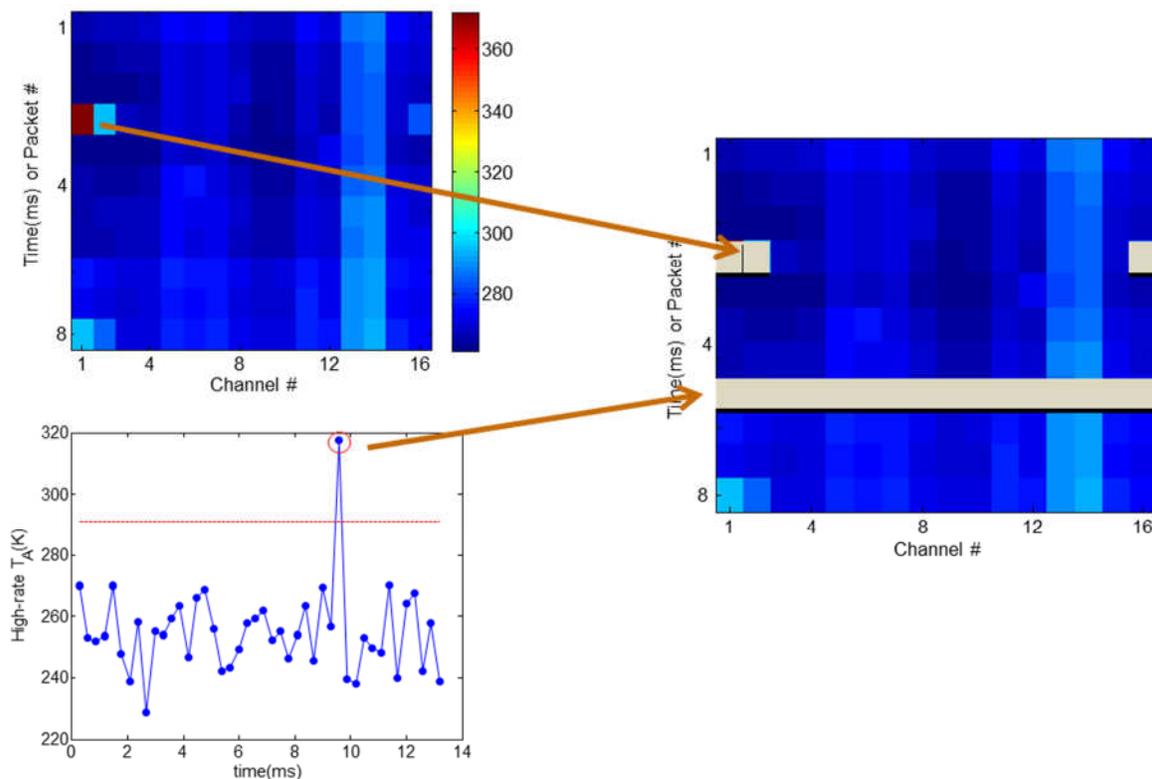
Figure 9.1: Illustration of RFI filtering process. Pixels detected in the sub-band

data stream (upper left) or fullband data stream (lower left) can flag portions of the 16 channel by 8 time sample spectrogram used to compute footprint brightness temperature.

There are nine RFI detection algorithms that can flag portions of the spectrogram:

Scenario	Action
Fullband pulse detection	Flag entire "rows" in the spectrogram
Fullband kurtosis	Flag entire "rows" in the spectrogram
Fullband third Stokes	Flag entire "rows" in the spectrogram
Fullband fourth Stokes	Flag entire "rows" in the spectrogram
Subband kurtosis	Flag single pixels in the spectrogram and adjacent frequency channels
Subband third Stokes	Flag single pixels in the spectrogram
Subband fourth Stokes	Flag single pixels in the spectrogram
Subband cross-frequency	Flag single pixels in the spectrogram and adjacent frequency channels
Subband integrated cross-frequency	Flag entire "column" of spectrogram and adjacent columns

Each detection algorithm has a detection threshold setting that determines its sensitivity and false alarm rate. Detection thresholds for each detector are specified in a settings file that is resolved on a 1-deg-by-1-deg global spatial grid, distinct for ascending/descending passes and fore/aft looks. For the beta release, all settings are uniform in space and for the ascending/descending/fore/aft cases, with one exception – the thresholds for the fullband pulse detector are increased (at 1-deg spatial resolution) for coastal regions, because the pulse detector may erroneously detect coastal crossings as RFI. Because precise calibration of the radiometer polarimetric channels was not a requirement for the beta release product, the polarimetric detection thresholds (i.e. fullband or subband third or fourth Stokes detectors) have been set very high so that the sensitivity for these detectors is very low. These settings will be revised in future product releases following validation of polarimetric channel calibration.

Because the L1B processor reports antenna temperatures both with and without RFI filtering, it is possible to determine the level of RFI detected (and removed) by SMAP. Figure 9.2 is an illustration of the "max hold" of horizontally polarized antenna temperatures compiled over the period Apr 1-8, 2015 on a regular 1-deg global grid. The "max hold" operation captured the maximum brightness temperature that occurred over the 8-day period, and is used to illustrate strong RFI events (which are easily distinguished from the geophysical background). The left plot of Fig. 9.2 is performed using antenna temperatures with no RFI filtering, while the right is performed after RFI filtering. The left image shows strong RFI sources (the anomalously high –

or red – regions of the image) particularly in Europe and Asia. The significant differences obtained in the right image illustrate that RFI filtering is reducing RFI corruption of SMAP data. However some strong sources remain even after RFI filtering, so that the beta release does contain unmitigated RFI in some situations. The project team is working to refine RFI filtering to eliminate or flag such regions in future versions of the L1B product.
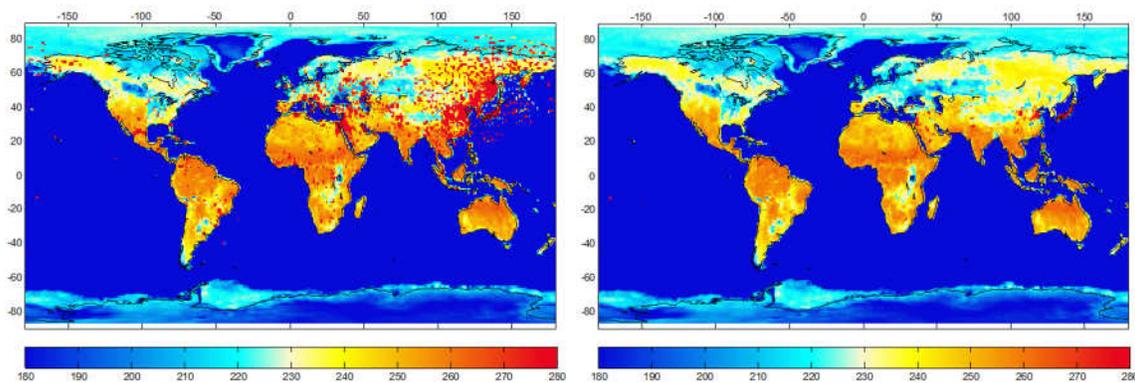
Figure 9.2: "Max hold" on a regular 1-deg global grid of horizontally polarized antenna temperatures (ascending passes, fore looks), before (left) and after (right) RFI filtering for the period Apr 1-8, 2015.

Figure 9.3 (upper left) is a zoom of Fig. 9.2 (left) in Eastern Asia; the results show strong RFI in Eastern China and over almost the entirety of Japan. The results again show significant reduction in corruption following RFI filtering (upper right), but Japan remains significantly impacted by RFI. The lower plot in Fig. 9.3 illustrates the max hold excluding any points removed by data quality flags. These flags remove much of the data over Japan, showing that data containing uncorrectable RFI is at least being excluded from further analysis in most cases. However some points remain that will required additional refinements to RFI filtering and flagging in future products. Detailed analyses are currently in progress for regions such as Japan in order to understand more completely the RFI sources in these regions and their properties. Initial results indicate that these sources are 'wideband' and occupy much of SMAP's bandwidth at all times (i.e. the entire 128 pixel spectrogram is corrupted.) Such RFI cannot be corrected by any of SMAP's RFI filtering procedures.
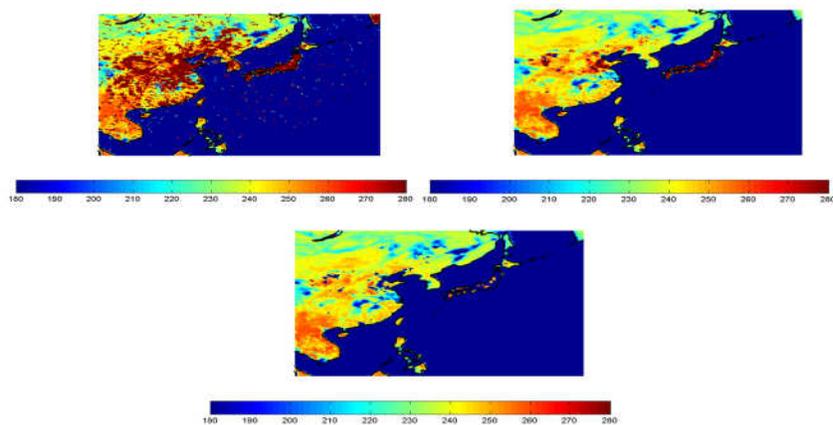
Figure 9.3: Zoom of Fig. 9.2 in Eastern Asia. (upper left) Max hold of horizontally polarized antenna temperatures prior to RFI filtering. (upper right) After RFI filtering. (lower) After RFI filtering and excluding any flagged data.

Figure 9.4 illustrates the detected RFI levels for ascending (left) and descending (right) passes for the period 5/1-5/8/15, again as a max hold in horizontal polarization. The results confirm the strong RFI observed in Europe and Asia. In this case, the color scale is reduced from Fig. 9.1 so that lower level RFI corruption (at the level of 10K or less) can be more clearly observed. Differences between ascending and descending passes also capture variations in RFI source transmissions with time of day and azimuth angle.
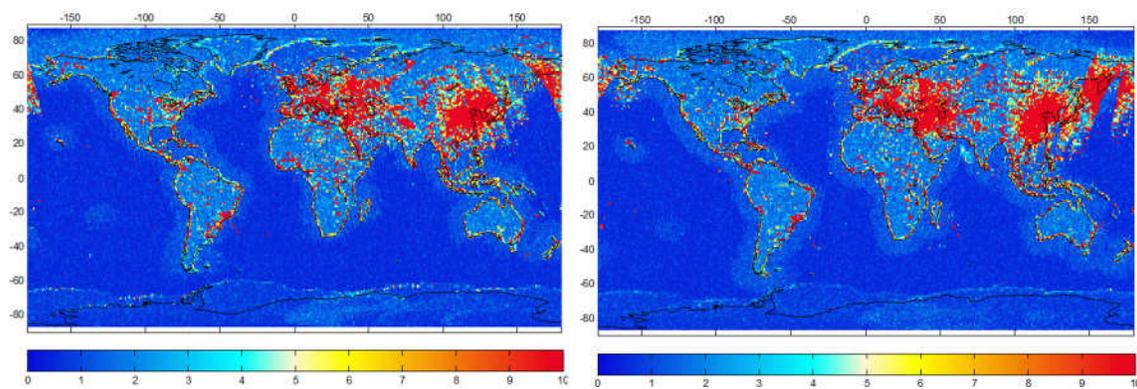
Figure 9.4: "Max hold" on a regular 1-deg global grid of horizontally polarized detected RFI, for ascending (left) and descending (right) passes, fore looks, for the period May 1-8, 2015.

Figure 9.5 illustrates the average fraction of the spectrogram flagged (i.e. out of 128 spectrogram pixels per footprint) on a global 1-deg grid. Obvious RFI sources are evident, but the ~5.5% false

alarm rate of the detection algorithm is also apparent when RFI sources appear to be absent. This detection rate implies that seven spectrogram pixels are flagged on average in the absence of RFI, causing degradation in radiometer sensitivity of the square root of 128/121, or 1.3 percent.
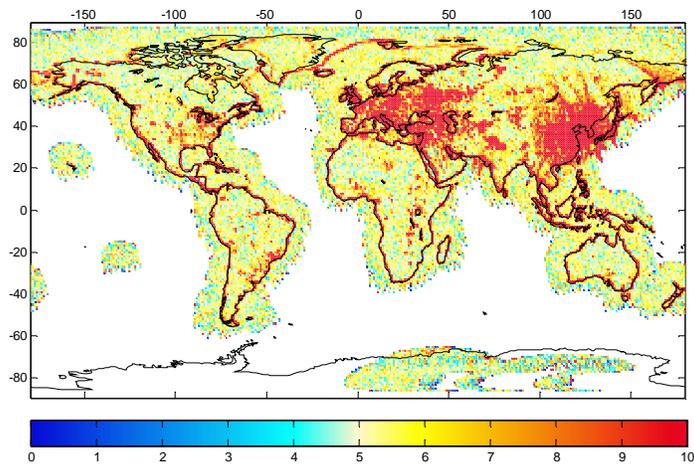
Figure 9.5: Average percentage of the 128 pixel spectrogram flagged on a global 1 deg x 1 deg grid in horizontal polarization (ascending fore looks) for the period Apr 1-8, 2015. The flagging of coastlines illustrated occurred in a pre-beta product release and has been corrected in the beta release by modifying detection thresholds for the fullband pulse detector.

These false alarm rates are near pre-launch expectations; the minor differences encountered will be addressed in future product releases. False alarm rates will be expected to increase slightly as well when the polarimetric detector sensitivity is activated.

Figure 9.6 provides additional information on overall brightness temperature and RFI statistics. The upper left plot is a complementary cumulative distribution function (CCDF) of horizontally polarized antenna temperatures over May 2015, including antenna temperatures prior to filtering, after filtering, and after filtering excluding flagged data.
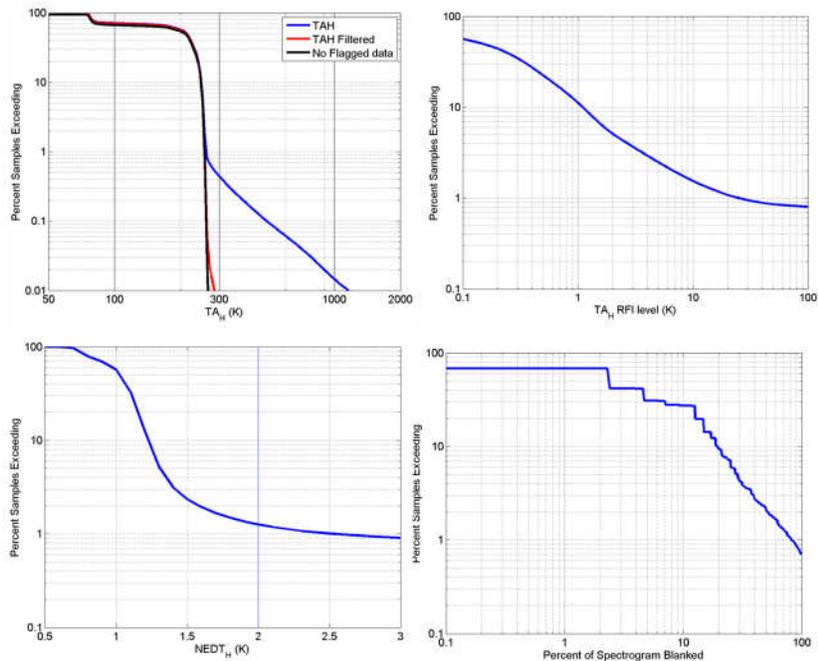
Figure 9.6: Summary statistics of SMAP horizontally polarized antenna temperatures for May 2015. (upper left) Complementary cumulative distribution function (CCDF) for antenna temperatures before RFI filtering, after RFI filtering, and after RFI filtering and flagging (upper right) CCDF of detected RFI levels (lower left) CCDF of NEDT following RFI filtering (lower right) CCDF of percentage of spectrogram flagged.

The results show the dramatic reduction in antenna temperatures greater than 300 K, indicating successful detection and filtering of large RFI sources. The upper right plot is a CCDF of the detected RFI level in horizontal polarization. The results show, for example, that ~ 1% of SMAP footprints are detected to have RFI levels of ~30 K or more, while ~ 10% of SMAP footprints have a detected RFI level of 1 K or more. The lower left plot is a CCDF of the radiometer sensitivity in horizontal polarization (NEDT) following RFI filtering. Approximately 98% of SMAP footprints have an NEDT < 1.6 K, while ~ 1.2% have an NEDT > 2 K. Footprints having NEDT greater than or equal to 2 K are flagged and excluded from downstream processing (as indicated by the vertical line in the figure). Finally, the lower right plot is a CCDF of the percentage of the spectrogram flagged, and shows that, for example, approximately 10% of SMAP footprints have 20% or more of the spectrogram flagged.

In general, the results obtained to date indicate that SMAP's digital backend and associated RFI detection and filtering algorithms are working successfully to improve the quality of SMAP brightness temperature measurements. However RFI corruption of SMAP data remains, in some cases sufficient to exclude large spatial regions from soil moisture retrieval. Beyond the results

shown, SMAP's digital backend produces a wealth of additional information on the frequency, time, and kurtosis properties of global L-band RFI sources. These data are being used to continue to refine RFI processing so that future product releases will achieve further improvements.

10 Fore and Aft Differences

This section discusses the comparison of geolocated temperature (antenna or brightness). The radiometric data are subdivided into ascending/descending orbits and into forward/backward looks. The data used represent one SMAP period of observations (8 calendar days) from 00:41:38 on May 3, 2015 to 00:45:51 on May 11, 2015. The data were first gridded on a regular 0.25-deg grid. For each pixel, the average, root-mean-squared, and the number of weighted 'hits' of the radiometric data were calculated. For a grid of spacing Q, the average signal T at each pixel (x,y) is given by:

$$T(x,y) = \frac{\sum_i T_i * W_i}{\sum_i W_i}$$

where T_i is the (antenna/brightness) temperature of the i-th footprint, the weight factors are given by:

$$W_i = \frac{^1/_{d_i}}{\sum_i {}^1/_{d_i}}$$

In this analysis, the following preliminary definition of d_i was adopted (more refined definitions will be explored in the future):

$$d_i \begin{cases} = \sqrt{(lat_i - y)^2 + (lon_i - x)^2} & \text{when } |(lat_i - y)| < Q \text{ and } |(lon_i - y)| < Q \\ = 0 \ \text{ elsewhere} \end{cases}$$

where the sum over i includes all available footprints.

When binning is done on a 0.25-deg grid, there are ~ 1.0e6 possible grid points over the Earth. Since each half-orbit file contains ~ 1.5e5 unique footprints, one full period of SMAP data (8 calendar days) produces > 15 'observations' of each grid point. In this time frame we observed these anomalies:

1) Orbit 1349 was not available
2) Files 1389_D and 1390_A showed abnormally high sea and land temperatures for a few scans near Antarctica and over Arabia
3) File 1404_D lost a few scans over North America
4) File 1442_D lost all its scans at mid-latitudes (less than 1/3 of the coverage is present)
5) File 1452_D lost coverage over Antarctica
6) Orbit 1453 had usable geolocation information for most of its scan

The robustness of the analysis was tested by creating, from the reported geolocation information, a corresponding set of control orbits. In these orbits, the radiometric data field is replaced by a number which represents the integration of a digital water fraction map (resolution 0.01 deg) with an elliptical Gaussian beam of the same HPBW as the SMAP's antenna; an ocean footprint has value of 1. The test-file reproduces all imperfections of L1B geometry information, but none of the (possible) inaccuracies from Solar/Lunar/Galactic/atmospheric/APC/Faraday corrections.

Fig. 10.1 shows the coverage map of the number of hits for a representative orbital geometry (descending orbits and fore looks), and the difference in the coverage for this and the corresponding combination (descending orbits and aft looks).
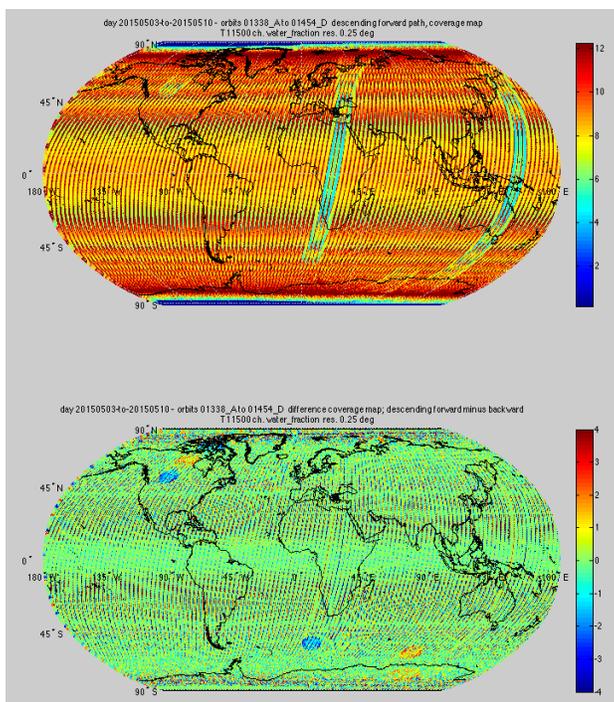
Figure 10.1: The number of hits for a representative orbital geometry over a 0.25-deg grid. Abnormal coverages over North America, the southern oceans and Antarctica were the results of the data anomalies (missing/incomplete files) listed in the text.

The result of the analysis for a water-fraction simulated observation map is shown in Fig. 10.2 for the same orbital geometry (descending-orbit and fore-minus-aft looks) described above. As expected, this difference map is remarkably featureless except along the coastlines, where the mismatch between the assumed antenna beam pattern and the one used to produce the data create a faint (about 1% of maximum signal) trace. It is worth highlighting that this trace can assume

positive or negative values at random, highlighting the fact that no systematic relation exists between the two antenna patterns.
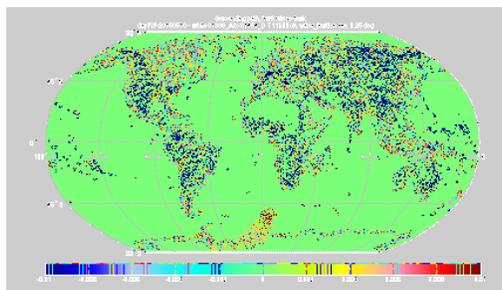
Figure 10.2: Units are water fraction. The feature seen in the southern hemisphere is an effect of a partially corrupted half-orbit.

The radiometric data, however, show a marked 'signature', which remains unchanged with polarization and rather depends upon the orbital direction. In Fig. 10.3 shows the analysis for descending orbits, front-minus-back looks. All coastlines facing east or south suggest that the backward looks record a warmer brightness temperature than the forward looks at the same spot, but west- and north-facing coastlines show the opposite effect.
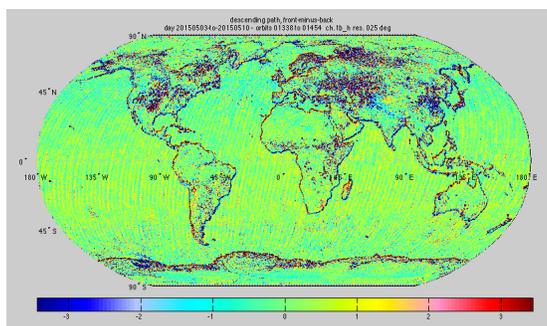
Figure 10.3: Difference in radiance between forward and backward looks for descending orbit. Striping on the oceans resulted from imperfect correction for reflected galactic contamination. Units are K.

This effect is common to both polarizations: when the Q component is considered, the effect is practically eliminated, as shown in Fig. 10.4:
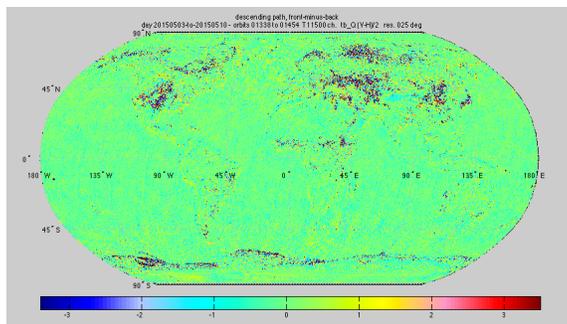
Figure 10.4: Difference between V-pol and H-pol for the differences in radiance between forward and backward looks for descending orbit. Units are K.

The African continent provides a good ensemble of coastlines facing open waters at multiple azimuths, as shown in Fig. 10.5.
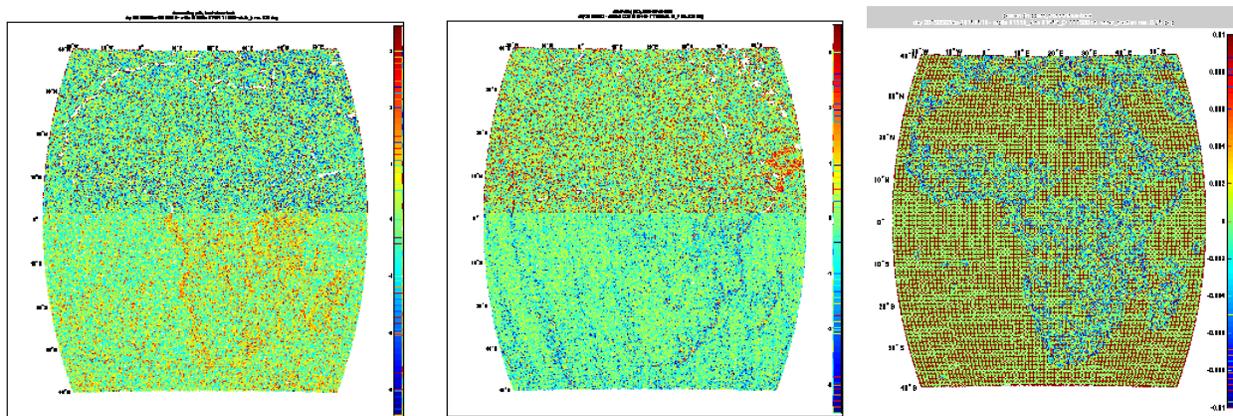
Figure 10.5: The radiometric differences for T_B (V-pol) produced by descending (left) and ascending orbits (middle). The sign change represented by the change in color at the coastlines is evident. When the same analysis was applied to the water fraction map (right), there was no dominant color (temperature bias) along any of the coastlines.

The following observations are evident in the analyses above:

1. There is an asymmetry in the front/back data.
2. The asymmetry is repeatable and shows approximately the same amplitude for antenna and brightness temperature fields.
3. These results are consistent in H-pol and V-pol and 4-pol and in the I-component. The effect almost disappears in the Q-component.

4. The cause of the effect is not a pointing error. The cause of the effect is common to all polarizations. The effect is consistent with an asymmetry in the antenna beam pattern, but it could well arise from some other agents.

This problem remains present in the beta-level and will be investigated further during the Cal/Val period.

11 Quality Flags

11.1 Implementation and Purpose

The full design of the L1B product is described in the SMAP Level 1B Radiometer (L1B_TB) Product Specification Document (SMAP Project, JPL D-72552, Jet Propulsion Laboratory, Pasadena, CA).

There are four quality flag data fields in the L1B product, one for each channel. These data fields are encoded in two-byte integers that, upon conversion into the respective 16-bit binary representations, indicate the effectiveness (or lack of it) of post-measurement correction performed to the antenna temperatures acquired by the radiometer. All four quality flags follow the same convention of bit usage:

- 0: A favorable condition was met in L1B TB processing
- 1: A favorable condition was not met in L1B TB processing

In addition, a '0' in the master bit (the least significant bit) indicates that a given TB sample is deemed to have acceptable quality. Table 11.1 lists the threshold values for key bit flags A summary definition of these quality flags is on the next page in Table 11.2.

Table 11.1: Threshold values for key bit flags in L1B_TB

Bit	Flag Name	Criterion	Threshold(s)	Units
1	Range flag	within	[0,335]	K
2	RFI detection flag	>	2	K
4	NEDT flag	>	2	K (rms)
5	Direct sun correction	>	200	sfu
6	Reflected sun correction	>	200	sfu
7	Reflected moon correction	≤	3	deg
9	Reflected galaxy correction	>	5	K

Table 11.2: Design of L1B_TB quality flag

Bit	Bit Definition	Interpretation
0	Quality	0: Brightness temperature measurement has acceptable quality. 1: Use of brightness temperature not recommended.
1	Range	0: Brightness temperature measurement falls in expected range. 1: Brightness temperature value is out of range.
2	RFI detection	0: RFI not detected. 1: RFI detected.
3	RFI correction	0: Either RFI was not detected, or the algorithm that removes RFI operated successfully. 1: If RFI was detected, the software was unable to correct the brightness temperature for RFI.
4	NEDT correction	0: Brightness temperature measurement has acceptable NEDT. 1: Use of Brightness temperature not recommended, since NEDT exceeds pre-determined threshold.
5	Direct sun correction	0: Correction for direct sun operated successfully on the brightness temperature. 1: Correction for direct sun did not function or yielded poor results on the brightness temperature.
6	Reflected sun correction	0: Correction for reflected sun operated successfully on the brightness temperature. 1: Correction for reflected sun did not function or yielded poor results on the brightness temperature.
7	Reflected moon correction	0: Correction for reflected moon operated successfully on the brightness temperature. 1: Correction for reflected moon did not function or yielded poor results on the brightness temperature
8	Direct galaxy correction	0: Correction for direct galaxy operated successfully on the brightness temperature 1: Correction for direct galaxy did not function or yielded poor results on the brightness temperature.
9	Reflected galaxy correction	0: Correction for reflected galaxy operated successfully on the brightness temperature. 1: Correction for reflected galaxy did not function or yielded poor results on the brightness temperature.
10	Correction for atmospheric condition	0: Correction for atmospheric conditions operated successfully on the brightness temperature. 1: Correction for atmospheric conditions did not function or yielded poor results on the brightness temperature.
11	Faraday rotation correction	0: Correction for Faraday rotation operated successfully on the brightness temperature. 1: Correction for Faraday rotation did not function or yielded poor results on the brightness temperature.
12	Null value	0: The corresponding brightness temperature element contains a calculated value. 1: The corresponding brightness temperature element is null.
13	Half orbit location	0: The corresponding brightness temperature lies within the half orbit specified in the file name. 1: The corresponding brightness temperature lies outside of the half orbit specified in the file name.
14	RFI check	0: The difference between unfiltered and RFI-filtered TA's is low enough to be acceptable. 1: The difference between unfiltered and RFI-filtered TA's is too large. The resultant brightness temperature likely remains contaminated with RFI.
15	RFI clean flag	0: The brightness temperature measure is free of RFI. 1: The brightness temperature measure is RFI contaminated.

12 L1C Gridded Product

12.1 Overview

The L1C TB product is derived from the L1B TB product, which represents calibrated, geolocated, time-ordered TB observations acquired by the radiometer. To generate the standard L1C product the processing software first ingests the L1B data. Based on the geometry and geolocation information, the ingested data are then re-mapped on a family of Earth-fixed grids using a gridding algorithm. The L1C data product is thus simply a gridded version of the L1B data product sharing the same major output data fields. Each product represents one half orbit, where the half-orbit boundaries are set at the southernmost and northernmost location of the spacecraft orbit path, separating ascending and descending orbit segments. Only those cells that are covered by the actual swath for a given projection are written in the product.

The L1C product presents the data in three projections at 36-km grid resolution (Section 12.2):

- Global Cylindrical projection ('M36' grid)
- North Polar projection ('N36' grid)
- South Polar projection ('S36' grid)

The projections are based on the NSIDC's EASE-Grid 2.0 specifications for SMAP (Brodzik, 2012). All elements in L1C are stored as HDF5 Datasets. Each projection corresponds to a separate HDF5 Group. Within each group, the data are provided in fore-looking and aft-looking views. Each set of looks contains TB observations, instrument viewing geometry information, and quality flags. The fore-looking set refers to information derived from the L1B observations acquired in the forward-looking portion of the scans when the antenna scan angle falls between 270 deg and 90 deg; the aft-looking set refers to information derived from the L1B observations acquired in the backward-looking portion of the scans. Only those cells that are covered by the swath for a given projection are written in the product. This organization is reflected schematically in Table 12.1.

Table 12.1: Fore- and aft-look data fields are stored separately in three projection groups.

L1C_TB					
N36 North Polar EASE-Grid 2.0		**M36 Global Cylindrical EASE-Grid 2.0**		**S36 South Polar EASE-Grid 2.0**	
Fore-looking	**Aft-looking**	**Fore-looking**	**Aft-looking**	**Fore-looking**	**Aft-looking**
1-D Array1	1-D Array1	1-D Array1	1-D Array1	1-D Array1	1-D Array1
1-D Array2	1-D Array2	1-D Array2	1-D Array2	1-D Array2	1-D Array2
1-D Array3	1-D Array3	1-D Array3	1-D Array3	1-D Array3	1-D Array3
:	:	:	:	:	:
1-D ArrayN	1-D ArrayN	1-D ArrayN	1-D ArrayN	1-D ArrayN	1-D ArrayN

12.2 EASE Grid

The EASE-Grid 2.0 has a flexible formulation. By adjusting one scaling parameter it is possible to generate a family of multi-resolution grids that "nest" within one another. The nesting can be made "perfect" in that smaller grid cells can be tessellated to form larger grid cells, as shown in Fig. 12.1.
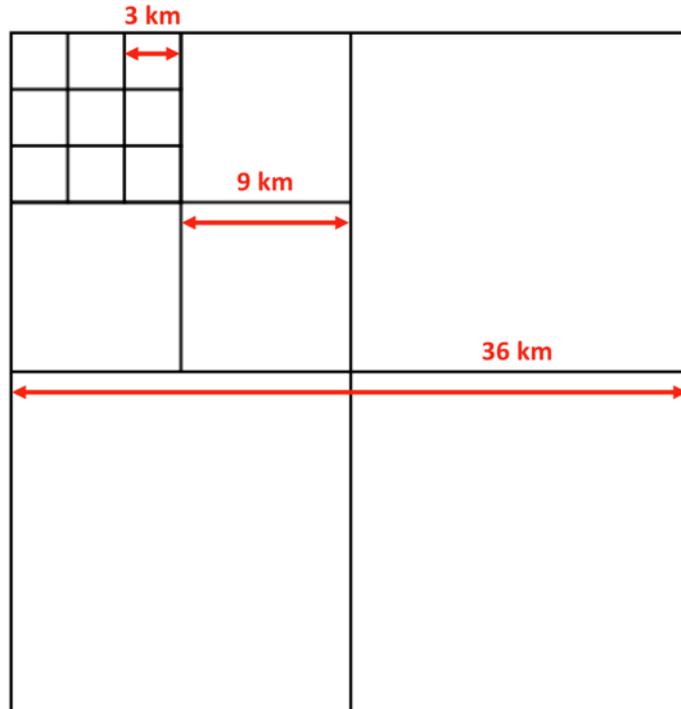
Figure 12.1: Perfect nesting in EASE-Grid 2.0 – smaller grid cells can be tessellated to form larger grid cells.

This feature of perfect nesting provides SMAP data products with a convenient common projection for both high-resolution radar observations and low-resolution radiometer observations, as well as their derived geophysical products. The three projections are illustrated in Fig. 12.2.

(a)   (b)

(c)
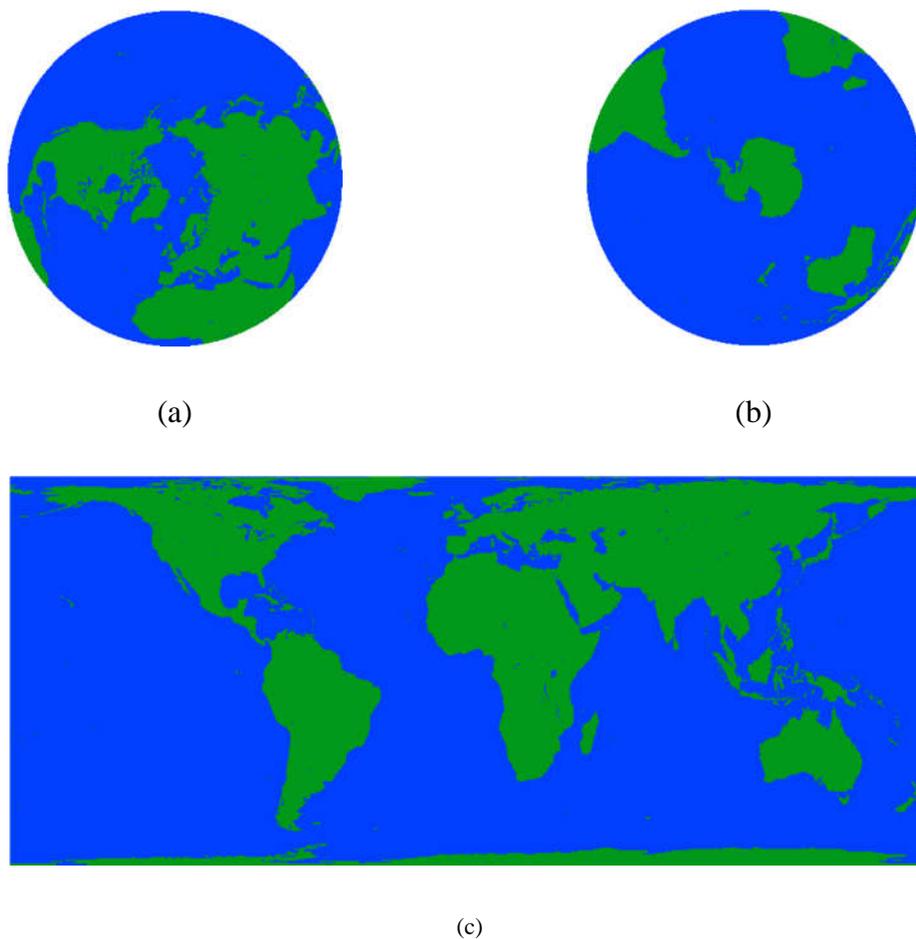
Figure 12.2: EASE-Grid 2.0 examples: (a) North Polar projection, (b) South Polar projection, and (c) Global Cylindrical projection. Figures credited to NSIDC.

12.3 L1C Output Fields

The L1C product inherits the majority of output fields of the L1B product. The output fields are separated into fore- and aft-looking subgroups in each EASE-2.0 Grid projection for both ascending and descending granules. Data fields are stored as one-dimensional arrays of size N, where N is the number of valid cells covered by the radiometer swath on the grid. Note that N varies with projections, but remains the same for both fore-looking and aft-looking views within a given projection. A detailed coverage of L1C data fields can be found in the Level 1C Radiometer Product Specification Document (SMAP Project, JPL D-72545, NASA Jet Propulsion Laboratory, Pasadena, CA., July 14, 2015).

Figures 12.3-6 show sample L1C images on Global Cylindrical, North Polar, and South Polar EASE-Grid 2.0 projections. Fore- and aft-look data are available in the product to enable radiometric analyses over regions where there is strong TB azimuthal dependence.
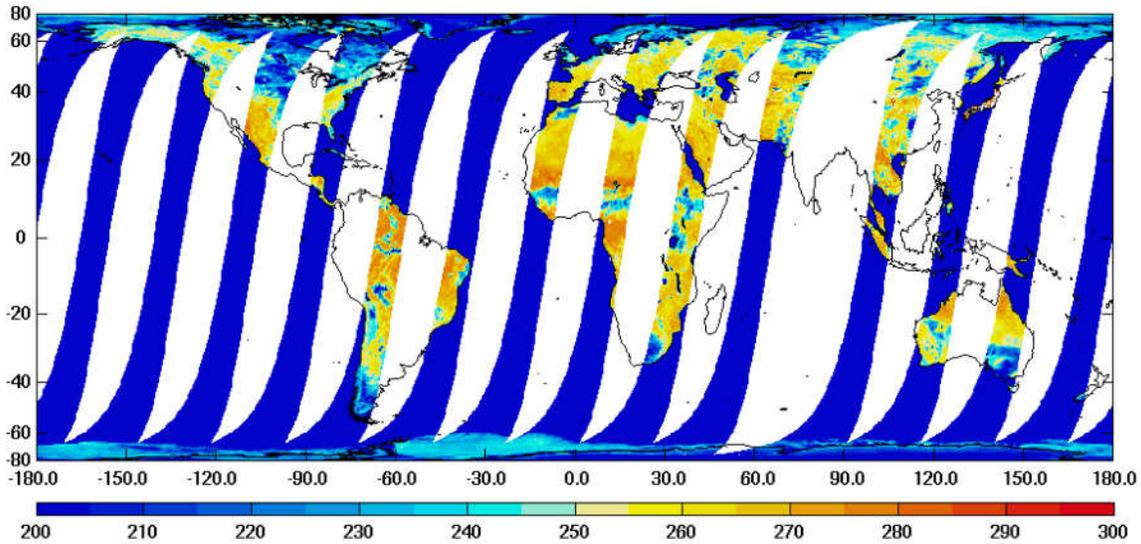
Figure 12.3: Descending fore-look H-polarized TB on Global Cylindrical EASE-Grid 2.0 projection.
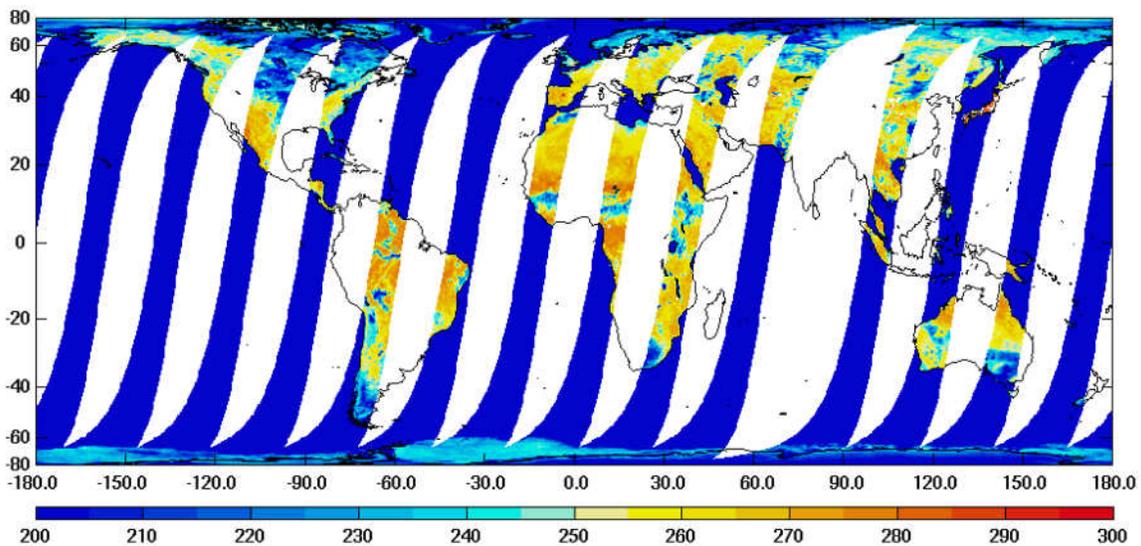
Figure 12.4: Descending aft-look H-polarized TB on Global Cylindrical EASE-Grid 2.0 projection.
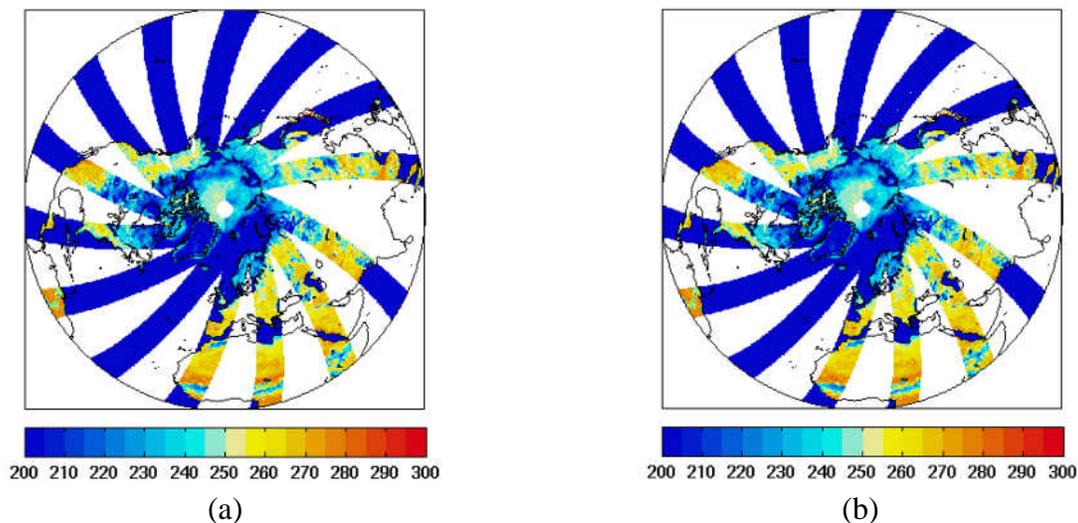
Figure 12.5: (a) Descending fore-look H-polarized TB on North Polar EASE-Grid 2.0 projection. (b) Descending aft-look H-polarized TB on North Polar EASE-Grid 2.0 projection.
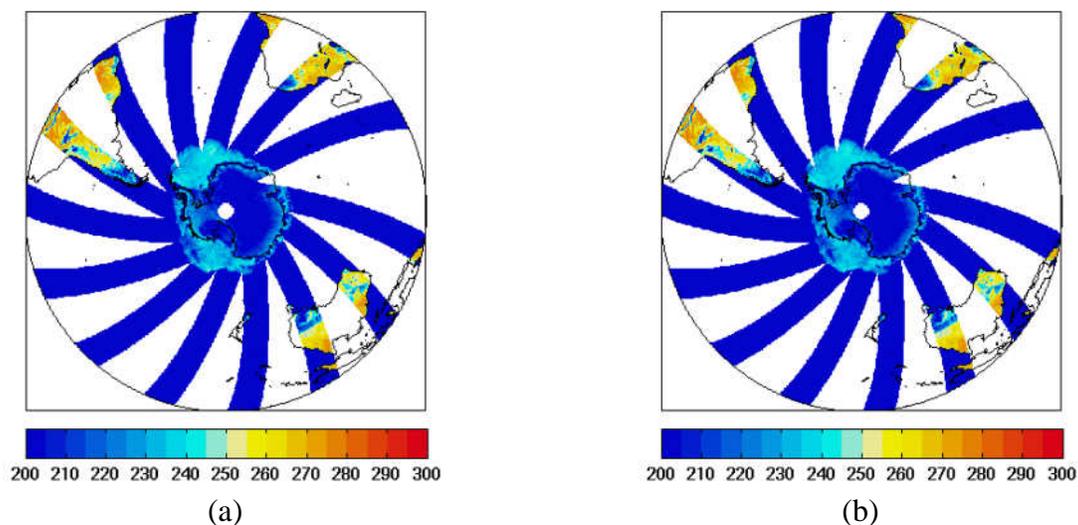
Figure 12.6: (a) Descending fore-look H-polarized TB on South Polar EASE-Grid 2.0 projection. (b) Descending aft-look H-polarized TB on South Polar EASE-Grid 2.0 projection.

Reference

Brodzik, M. J., B. Billingsley, T. Haran, B. Raup, M. H. Savoie. "EASE-Grid 2.0: Incremental but Significant Improvements for Earth-Gridded Data Sets," *ISPRS International Journal of Geo- Information*. 2012; 1(1): 32-45.

13 Future Work

Though the beta release brightness temperature values are very close to expected values over the ocean, land, ice and cold-sky – minor adjustments with respect to the APC, noise-diode and front-end loss still need to be need. Going forward we will adjust the following parameters in the final release product:

1. APC spillover – Requires a cold-sky measurement with an ocean to land back-lobe transition. Spillover can act as a gain term that needs to be calibrated out first.
2. APC cross-pol – This correction requires a model for the ionospheric rotation model, ocean model, unpolarized nadir views or rainforest views for full calibration.
3. Gain/Offset adjustment – Minor gain adjustments will be made based off results from the Antenna spillover correction. The cold-sky and ocean will be used to incorporate all corrections together. The noise-diode temperature values and reference load values will be varied.
4. 3rd Stokes calibration – This calibration is done based off cold-sky and ocean measurements observed, and the cold-sky maneuvers performed.
5. 4th Stokes calibration – This calibration is done based off land and ocean 4th Stokes signatures observed.
6. RFI threshold $3^{rd}/4^{th}$ Stokes – The RFI threshold values for $3^{rd}/4^{th}$ Stokes based algorithms will be updated after final Stokes characterization.
7. Drift characterization – Currently drift correction is via noise-diode temperature changes. We will assimilate a couple of months of data over the ocean, Antarctica and cold-sky to characterize the type of drift observed and correct it accordingly.
8. Reflector/radome sensitivity – The front-end loss sensitivity due to the radome and reflector components of the SMAP instrument will be updated based on results obtained from the eclipse data of SMAP (May to August).
9. Gain filter – The gain averaging filter will be updated over the next couple of months to properly account for systematic 1/f noise currently observed in the averaged data.

Acknowledgment